Electronic Supporting Information

Mn_2CoReO_6: A Robust Multisublattice Antiferromagnetic Perovskite with Small A-Site Cations

Corey E. Frank,[a] Emma E McCabe,[b] Fabio Orlandi,[c] Pascal Manuel,[c] Xiaoyan Tan,[d] Zheng Deng,[e] Mark Croft,[f] Vanessa A. Cascos,[b] Thomas Emge,[a] Hai L. Feng,[a] Saul Lapidus,[g] Changqing Jin,[e] MeiXia Wu,[h] Man Rong Li,[h] Steven Ehrlich,[i] Syed Khalid,[i] Nicholas Quackenbush,[j] Shuang Yu,[e] David Walker,[k] and Martha Greenblatt*[a]

1) Detailed Motivations

The seminal double perovskite oxide ($A_2BB'O_6$) with potential spintronic or other room temperature applications, Sr_2FeMoO_6, was discovered by Kobayashi et al. and has large magnetoresistance, high magnetic transition temperature (418 K), and completely polarized conduction band.[1, 2 3, 4] This exciting discovery inspired many more researchers to investigate DPs in the decades since, and progress is still made in designing and synthesizing new materials in this versatile structure type. Interesting examples of double perovskite oxides (DPs) with potential spintronic applications, a large *A*-site cation, a 3d metal on the B site, and a 4d/5d B' transition metal, include Ba_2FeMoO_6 (Tc = 340 K)[5] and Sr_2FeReO_6 (Tc = 415 K),[6] two above room temperature magnetoresistant materials. Despite a difference in 4d/5d conduction band electrons when compared to Sr_2FeMoO_6, Sr_2FeReO_6 (Tc = 415 K) shows a magnetoresistance of up to 7% at 7 T and 300 K.[6] Interesting magnetic properties in these materials are attributed to double-exchange or super- exchange interactions between the B and B'-cations, and so strategies to tune properties are generally directed to changing the occupancies of these two sites while maintaining a late transition metal on the B'-site to promote spin orbit coupling and spin polarization.[7, 8] Potential candidates for new room-temperature spintronic materials need to be carefully chosen.

In a DP, three types of order are typically seen between the B and B'-site cation octahedra that surround the large (12-coordinated) A cation polyhedra: rock salt, layered, or disordered. This is generally governed by the degree of difference in size and charge between the B and B' cations.[9] For example, in recently investigated antiferromagnetic A_2CoReO_6 perovskites (A = Ba^{2+}, Pb^{2+}, Sr^{2+}), the size and charge differences between Co^{2+} (0.745 Å) and Re^{6+}(VI) (0.55 Å) are sufficiently large that the B and B' cations fully order in a rock salt configuration.[10-12] Pb_2CoReO_6 is particularly interesting because it exhibits bulk antiferromagnetic order (T_N= 16 K) combined with local ferro-or-ferrimagnetic interactions and a negative magnetoresistance of -23% at 10 K (H = 9 T).[11]

The rule of thumb that predicts stability of perovskite structure-type compounds is the Goldschmidt tolerance factor, ($t = \frac{R_A + R_O}{\sqrt{2(R_B + R_O)}}$), which corresponds to the ratios of the radii of the A and B cations and the oxygen anions.[13, 14] An ideal perovskite will have a cubic structure with t = 1, however, the BO_6 and $B'O_6$ octahedra can tilt and distort to accommodate A cations with a less-than-perfect tolerance factor. [15] Exceptions exist, as in the case of double corundum Ni_2MnTeO_6, but generally double perovskites with t < 0.85 are unlikely to form under ambient pressure conditions. Instead, DPs with small *A*-site cations tend be metastable and, as mentioned in the main text, require high pressure and temperature to form.[16]

The two first transition metal-only $A_2BB'O_6$ perovskites reported were synthesized at high pressure and temperature, Mn_2FeReO_6 and Mn_2MnReO_6, both crystallize in the distorted monoclinic $P2_1/n$ space group. Mn_2FeReO_6 was reported by our group in 2015 to be a half-metallic ferrimagnet with giant magnetoresistance (220%) at 5K.[17] Its isostructural analogue, Mn_2MnReO_6demonstrated no magnetoresistance.[22] The lack of magnetoresistance in this compound was attributed to the

antiferromagnetic coupling of the A and B site magnetic sublattices.[18, 19] These compounds were independently discovered at approximately the same time by Arévalo-Lopez *et al*. with similar properties, who assigned the Mn *A*-site cations a full 12 O-coordination, despite four of the Mn-O bonds being unusually long. In contrast, our group assigned only eight coordination of Mn-O bonds at the Mn *A*-site.[20]

Further complicating matters of synthesis: often it is *corundum* $A_2BB'O_6$, not perovskite, which is the thermodynamically stable structure even at high pressure. Stabilizing the double perovskite of a particular composition typically requires even higher applied pressure.[21, 22] Unfortunately for the synthetic chemist, it is not possible to predict a priori which conditions will stabilize the double perovskite phase; the exact conditions and relative stabilities of the structures are both highly dependent on composition.

Recently, our group also published the structural and magnetic properties of $Mn_2(Fe_{0.8}Mo_{0.2})MoO_6$, the third known transition-metal-only double perovskite oxide.[23] $Mn_2(Fe_{0.8}Mo_{0.2})MoO_6$, a line phase of the polar ferrimagnetic double corundum Mn_2FeMoO_6[24] (space group *R3*, T_c = 337K), illustrates well the aforementioned difficulty of predicting the stable structure of a given compound. Both the parent compound and the line phase are synthesized at 8 GPa and 1623 K, so it clearly cannot be simply synthetic conditions which are key to the formation of double perovskite vs corundum in this case. In Mn_2MnReO_6 and Mn_2FeReO_6, the stabilization of a double perovskite phase over double corundum was attributed to the specific spin-structures of each compound, combined, perhaps, with spin-orbit coupling from Re on the B'-site.[17, 18] As $Mn_2(Fe_{0.8}Mo_{0.2})MoO_6$, is the only known line phase of $Mn_2(Fe_{1-x}Mo_x)MoO_6$, its formation suggests a "synergy" of spin and crystal structure and thermodynamics. Presently, finding more of these types of compounds are of interest to reveal the underlying principles that govern the formation and properties of these complex structures.

As emphasized in the main text, this work presents the fourth known transition-metal only DP with small *A*-site cations, Mn_2CoReO_6. Like its predecessors, Mn_2CoReO_6 crystalizes in the $P2_1/n$ space group, and like Mn_2MnReO_6 and A_2CoReO_6 (A = Ba, Pb, Sr) compounds it exhibits long range antiferromagnetic (AFM) order.[10-12, 18, 19] The AFM character of the initial transition is exceptionally robust, persisting at fields of up to 7 T (Figure 2 (main text)). In the main text, and here in further detail, we describe the nuclear and magnetic structures and the magnetic and magnetotransport properties of Mn_2CoReO_6.

2) Experimental Details

Synthesis: Small (< 0.1 mm) black, plate-like crystals of Mn_2CoReO_6 were synthesized at high pressure and temperature in a Walker-Type multi-anvil device. Stoichiometric amounts of MnO (99%, Sigma-Aldrich), Co_3O_4 (99.9985%, Alfa Aesar), Re (Strem Chemicals, 99.99%), and ReO_3 (Alfa Aesar, 99.9%) were thoroughly ground in an agate mortar and sealed in a platinum capsule. The ReO_3 was stored in a 200 ^oC drying oven, and the Co_3O_4 was dried overnight at 700 ^oC before being ground, as both are mildly hygroscopic. The capsule was pressurized to 8GPa and heated at 1623 K for 30 min before being quenched to room temperature by turning off power to the resistance furnace. The pressure was maintained throughout the heating and quenching process, then slowly decompressed over 8-12 hours.

Specific Heat Capacity: Specific heat capacity (Cp) was measured on a PPMS by Quantum design with Heat Capacity Option 2.7.2 Build 2. A small pressed pellet sample weighing 27.3 mg and roughly cylindrical in shape was measured between 2 and 150 K in zero magnetic field.

X-ray and Neutron Diffraction: Single crystal X-ray data (SCD) were collected with Mo K_α, λ = 0.7107 Å, at room temperature on a single crystal 0.040 x 0.020 x 0.010 mm^3 on a Bruker Smart APEX system

with charge-coupled device (CCD) area detector and mono-capillary collimation. The structure was solved with the SHELXT-2014/15 and refined with SHELXL-2014/7 software packages with data reduction performed in BRUKER APEX 3 and SAINT. [25,26,27,28]

Room temperature powder X-ray diffraction (PXRD) data were collected at room temperature on ground crystals of Mn_2CoReO_6 with a Bruker D8 Advance Diffractometer with a SOL-X solid state detector (Cu K_α, λ = 1.5418 Å).

Room temperature synchrotron powder X-ray diffraction (SPXD) data were collected at Argonne National Laboratories on the high energy beamline 11-ID-C (λ = 0.1173 Å). The ground sample was sealed in an evacuated quartz ampule and measured without being removed.

For Powder Neutron Diffraction (NPD), approximately 100 mg of sample were transferred to a cylindrical, thin-walled vanadium can inside a glovebox and quickly loaded into a CCR and evacuated. A high quality NPD scan (80 μAmp hr) was collected at 2 K and shorter scans (16.7 μAmp hr) collected every 5 K on warming to 135 K. Data were analyzed with the TopasAcademic software[29] and ISODISTORT[30] was used to explore possible magnetic structures and to give a description of the magnetic structures in terms of the nuclear structure and symmetry-adapted magnetic modes. (ISIS data available at DOI: 10.5286/ISIS.E.101137712)

X-ray Absorption Near-Edge Spectroscopy: Mn-K, Co-K and Re-L_3 X-ray absorption near edge spectroscopy (XANES) data were collected in both the transmission and fluorescence mode with simultaneous standards. All of the spectra were fit to linear pre- and post-edge backgrounds and normalized to unity absorption edge step across the edge. The title compound XANES spectra were collected at the QAS, 7BM Beamline at NSLS-II using a Si(111) channel-cut monochromator in the "qick", continuous scanning mode. Some of the standard spectra were previously collected on beam line X-19A at NSLS-I with a Si-111 double crystal monochromator. Selected standard spectra were also collected at NSLS-II 6BM taken with a Si (311) monochromator. It should be noted that the Mn_2CoReO_6 samples were prepared and packaged for transport to NSLS-II in a sealed nitrogen gas container. Moreover, the actual XANES measurements were performed with the sample in a sealed nitrogen gas bag mounted in the beam.

Scanning Electron Microscopy-Energy Dispersive X-ray Spectroscopy: Scanning electron microscopy-energy dispersive X-ray spectroscopy (SEM-EDX) images were generated with a Ziess-Sigma Field Emission SEM with Oxford INCA Energy 250 Microanalysis system. A fragment of as-made Mn2CoReO6 was embedded in epoxy resin and ground so that there was a flat surface. The sample was then coated in a thin (3-10 nm) coating of carbon before being loaded into the SEM-EDX system for analysis. Measurements were performed at a working distance of 8.5 mm and an accelerating potential of 15 KeV.

Magnetism and Magnetotransport: Field Cooled (FC) and Zero Field Cooled (ZFC) magnetic measurements were carried out with a SQUID magnetometer in a temperature range of 5 - 400 K with an applied magnetic field of 0.5 T. At H = 0.1 T, FC and ZFC data were collected at a temperature range of 5 – 300 K. At H = 1, 2, 3, 5, and 7 T, FC and ZFC data were collected at a temperature range of 5 – 135 K. Isothermal magnetization curves were obtained at 5, 100, 150, and 300 K under an applied magnetic field which ranged from 6 T to -6 T.

Magnetotransport measurements were performed on a pressed pellet sample of Mn_2CoReO_6 crystals with the standard four-probe technique in a Quantum Design physical property measurement system (PPMS) at fields of 0 and 7 T.

3) Preliminary characterization

Optical Analysis: A fragment of the as-made densely packed pellet of Mn_2CoReO_6 crystals and crystallites were embedded in epoxy resin before being ground and polished for analysis (Figure ESI3.1). Optical analysis resulted in a doubly-polarized incident illumination image which indicates that the sample is an approximately pure (> 90%) single phase. Dark grey crystallites are posited to be a Mn-rich contaminate phase, whereas the lighter, more irregular-edged crystallites are likely Re-rich oxides. The sharp grain boundaries between Mn_2CoReO_6 crystals are also apparent. Optical analysis is a useful tool for early phase identification and evaluation of synthetic conditions, however it should be noted that the initial estimates are simply that, and the sample must be evaluated by a precise analytical technique such as PXRD (Figure ESI3.2) to accurately assess sample composition.

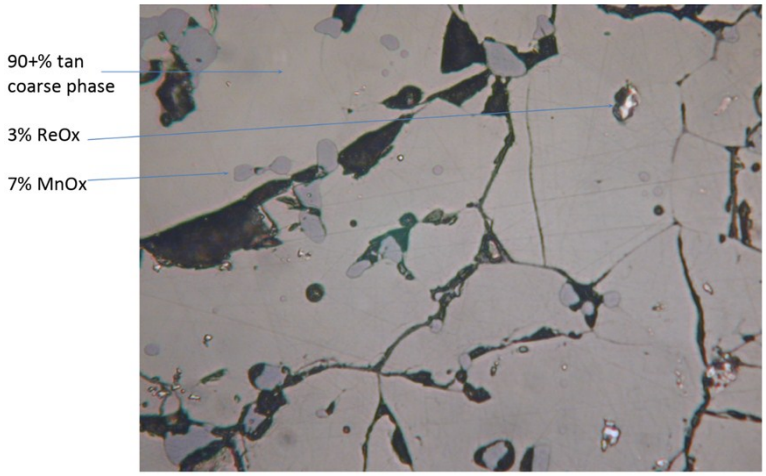

Figure ESI3.1 Doubly-polarized incident illumination image of Mn_2CoReO_6 embedded in epoxy resin.

Powder X-ray Diffraction (PXRD): PXRD data were collected at room temperature on ground crystals of Mn_2CoReO_6 and were initially compared to known transition-metal-only double perovskites Mn_2MnReO_6 and Mn_2FeReO_6 (Figure ESI3.2).[17-19] Mn_2CoReO_6 peaks are well indexed in space group 14 ($P2_1/n$) when compared to these known samples, with trace impurities not perceptible by laboratory X-ray. This space group is distinguished from similar space groups (such as *Pnma*, $P2_1/a$, or $P2_1/c$) by the rock salt ordering of the BO_6 and $B'O_6$ octahedra and by the octahedral tilting scheme. As it is typical of double perovskites, in Mn_2CoReO_6 the B and B' cations are each surrounded by six oxygen atoms. Atypically, the Mn *A*-cations are 8 coordinated, rather than twelve, due to significant B and B' octahedral tilting necessitated by the small atomic radii of the *A*-cations. This feature is consistent with the *A*-cation environments and also observed in the previously reported transition-metal-only double perovskites.

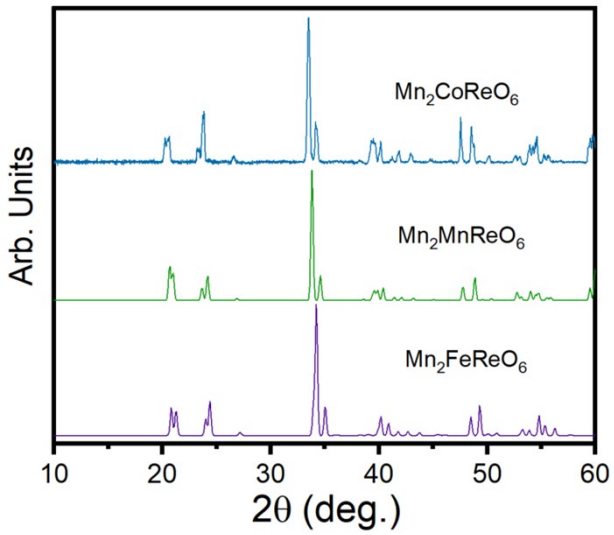

Figure ESI3.2 Laboratory PXRD data for Mn_2CoReO_6 compared with scans of $P2_1/n$ Mn_2MnReO_6 and Mn_2FeReO_6 calculated from literature.

Single Crystal X-ray Diffraction(SCD): Room temperature SCD refinements (details in Table ESI3.2) indicate that Mn_2CoReO_6 crystalizes in the highly distorted monoclinic space group $P2_1/n$ with a = 5.2356(2) Å b =5.3536(2) Å, c = 7.6330(3) Å, β = 89.9627(19). Based on electron densities from SCD, the B site refines to 97.6(2)% Co and 2.4(2)% Re, with a coordinating result for the majority-Re B' site.

According to SCD, the average bond lengths of <Re-O> (1.928(3) Å) are somewhat smaller than those found in Mn_2FeReO_6 (1.961(9) Å), where Re is in oxidation state 5+ (d^2),[17] but closer to those in Mn_2MnReO_6 where the Re valence is a mixture of V and VI (1.930(2) Å).[18] The slightly shortened <Re-O> bond distance in Mn_2CoReO_6 compared to analogous Mn_2MReO_6 perovskites can reasonably be attributed to the fact that the B' site of Mn_2CoReO_6 is wholly populated by d^1 Re(VI), while the other two structures show either ~d^2 Re(V) or a mixture of ~$d^{1/2}$ Re(VI/V), respectively. Bond valence sum (BVS) calculations for Mn_2CoReO_6 support this interpretation, and indicate formal oxidation states of $Mn^{2+}{}_2Co^{2+}Re^{6+}O_6$ (Table ESI3.1), which have been confirmed by X-ray absorption near edge spectroscopy (*vide infra*).

As can be clearly seen in Figure ESI3.3, *B/B*' octahedra are extremely tilted (tilt scheme of a- a- c+ in Glazer notation)[31]with a concomitant decrease in symmetry when compared to perovskites with no (or less severe) octahedral tilting. The Re-O-Co superexchange bond angles around the oxygen are 141.03(17) °, 137.18(16) °, and 139.07(14) °, respectively. These are much smaller than what was previously observed in Sr_2CoReO_6 (180.0°, 165.97(9) °, 173°), which had a tilt magnitude of 7.0° for the CoO_6 octahedra. The octahedra in Mn_2CoReO_6 must tilt much more severely in order to accommodate a smaller *A*-site Mn^{2+} cation. The magnitude of octahedral tilting, ϕ, can be calculated with the formula ϕ ° = (180 – θ)/2 where θ = Co-O(2)-Re angle.[12] In Mn_2CoReO_6, ϕ of the CoO_6 octahedral tilting is 21.4 °, three times greater than that of the sister compound Sr_2CoReO_6.

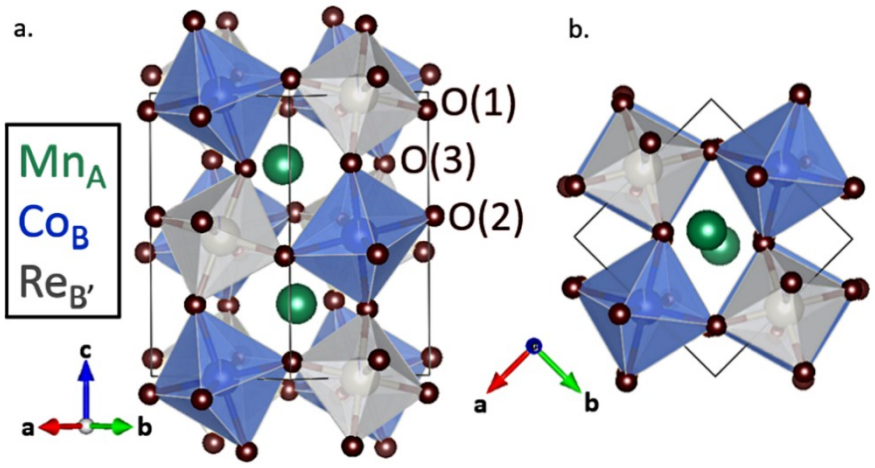

Figure ESI3.3 Illustration of the $P2_1/n$ double perovskite structure of Mn_2CoReO_6, viewed along the A-B plane, as found by SCD. The Mn eight-coordinated *A*-site cations are represented in green and the CoO_6 and ReO_6 *B/B'* octahedra, in an a-a-c+ tilt scheme, are blue and grey, respectively. Oxygen atoms are represented in red.[32]

Table ESI3.1. Selected Bond Distances (Å) and Bond Valence Sums (BVS) for Mn_2CoReO_6 at room temperature.

MnO_8		CoO_6	
Mn - O1	2.120(4) Å	Co -O1 x2	2.043(4) Å
	2.619(4) Å	-O2 x2	2.128(3) Å
	2.635(4) Å	-O3 x2	2.111(3) Å
-O2	2.590(3) Å	<Co-O>	2.094(3) Å
	2.729(4) Å	BVS	2.035
	2.123(3) Å		
-O3	2.103(3) Å	ReO_6	
	2.169(3) Å	Re -O1 x2	1.929(3) Å
<Mn-O>	2.386(4) Å	-O2 x2	1.892(3) Å
BVS	2.007	-O3 x2	1.963(3) Å
		<Re-O>	1.928(3) Å
		BVS	6.746

Table ESI3.2. Select details of the single crystal structural refinements.

Empirical Formula	Mn_2CoReO_6
Formula Weight	451.01 g/mol
Temperature	571(2) K
Wavelength	0.71073 Å
Crystal System	Monoclinic
Space group	$P2_1/n$ (14)
Unit cell dimensions	a = 5.2356(2) Å
	b = 5.3536(2) Å
	c = 7.6330(3) Å

	α = ϒ = 90 °
	β = 89.9627(19)°.
Volume	213.948(14) Å^3
Z	2
Density (calculated)	7.001 Mg/m^3
Absorption coefficient	37.715 mm^{-1}
Crystal size	0.040 x 0.020 x 0.010 mm^3
Theta range for data collection	4.651 to 45.267°.
Reflections collected	5485
Independent reflections	1774 [R_{int} = 0.0722]
Completeness to theta = 25.242°	99.0 %
Goodness-of-fit on F^2	0.705
Final R indices [I>2sigma(I)]	R1 = 0.0248, wR^2 = 0.0474
R indices (all data)	R1 = 0.0364, wR^2 = 0.0512
Extinction coefficient	0.0061(3)
Largest diff. peak and hole	$\Delta\rho_{max}$ = 1.928 eÅ^{-3} and $\Delta\rho_{min}$ = -2.899 eÅ^{-3}

Scanning Electron Microscopy-Energy Dispersive X-ray Spectroscopy (SEM-EDX): In order to elucidate the molar ratio of composition, SEM-EDX was used. SEM-EDX is a semi-quantitative technique,[33, 34] and thus can be used in concert with high sensitivity diffraction techniques (such as single crystal and neutron diffraction) to confirm a refined ratio. First, an element map was generated which showed one large main phase and some inclusions of two other phases, which look "dark" or "bright" on the black and white SEM image. In the SEM-EDX map, the "dark" spots appear to be Re deficient and Co/Mn rich. Analysis of the targeted main phase implies an Mn:Co:Re ratio of 2:1:1, which, combined with high quality diffraction refinements confirms that the compound of interest in this paper is indeed Mn_2CoReO_6.

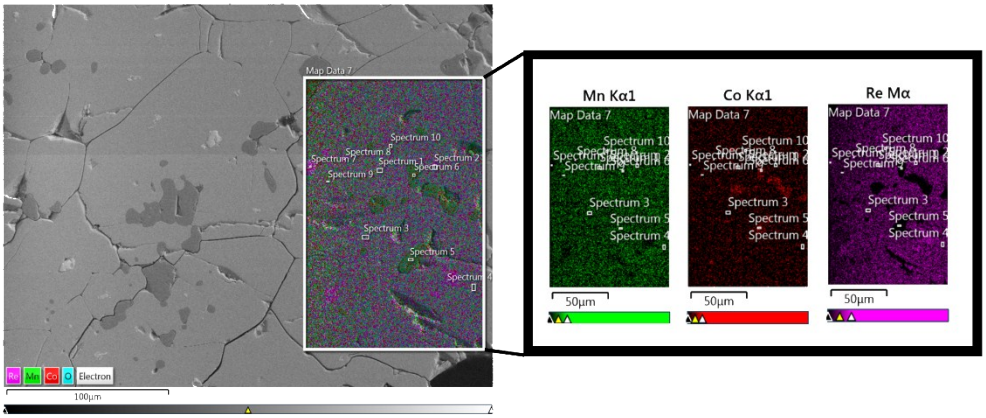

Figure ESI3.4. SEM image of Mn_2CoReO_6 with EDX map overlated. Mn, Co, and Re are represented in green, red, and pink, respectively. The Mn/Co rich and Re defficient impurity can be clearly seen in the individual element maps. The ratio of Mn: Co: Re indicated by this technique is 2:1:1.

4) Nuclear structure at 200 K from Neutron Powder Diffraction (NPD):

NPD data collected at 200 K were used to investigate the nuclear structure of Mn_2CoReO_6 and the main peaks were consistent with the $P2_1/n$ ($a^-a^-c^+$) structure reported for Mn_2FeReO_6,[17, 35] with a trace of a spinel-like impurity phase (such as Mn_3O_4 or $Mn_{3-x}Co_xO_4$).[36] The good contrast in neutron scattering lengths of the cations (Mn = -3.73(2) fm, Co = 2.50(3) fm, Re = 9.2(2) fm)[37] means that NPD data are sensitive to antisite disorder. Refinements using a single global temperature factor and

constraints to maintain sample composition revealed almost complete ordering of Co and Re on the perovskite *B* sites (referred to as Co_B and Re_B), and ~16% disorder between Mn on the *A* site (Mn_A) and Co on the *B* site and this cation distribution was fixed in subsequent refinements. The stoichiometry with respect to oxygen was checked by allowing the occupancies of oxygen sites to refine (whilst the Re site occupancy was fixed); this suggested a small level of oxygen vacancies. These site occupancies were then fixed in subsequent refinements. Refinement details, bond lengths and angles are given in Tables ESI4.1 and 2. Refinement profiles are given in Figure ESI4.1. The average Re – O bond length is longer than that reported at 200 K for Mn_2MnReO_6,[18] perhaps indicating a lower oxidation state for this site. Likewise, the Mn_A coordination sphere is also larger than that in Mn_2MnReO_6, despite the 8% Co occupancy, suggesting that the manganese is predominantly in the 2+ oxidation state.

Table ESI4.1 Refinement details from Rietveld refinement of Mn_2CoReO_6 using 200 K NPD data in space group $P2_1/n$ with a = 5.2366(1) Å, b = 5.3498(1) Å, c = 7.6311(1) Å, β = 89.926(2)°; R_{wp} = 3.45%, R_p = 5.02% and χ^2 = 2.02.

Atom	**site**	***x***	***y***	***z***	**Factional occupancy**	**U_{iso} × 100 (Å^2)**
Mn_A/Co_A	4*e*	0.4917(4)	0.5496(4)	0.7478(5)	0.9197(9)/ 0.0803(9)	1.33(6)
Co_B/Mn_B	2*c*	0	0.5	0	0.8394(9)/ 0.1606(9)	1.33(6)
Re_B	2*d*	0.5	0	0	1	0.09(3)
O(1)	4*e*	0.3401(3)	0.3060(3)	0.9296(3)	0.940(4)	1.19(8)
O(2)	4*e*	0.3118(3)	0.3182(3)	0.5564(3)	0.985(4)	0.57(7)
O(3)	4*e*	0.8783(2)	0.4343(2)	0.7375(3)	0.965(2)	0.46(4)

Table ESI4.2 Selected bond lengths and angles from Rietveld refinement of Mn_2CoReO_6 using 200 K NPD data in space group $P2_1/n$.

Bond	**Length (Å)**	**Bond**	**Length (Å)**
Mn_A/Co_A – O(1)	1 × 2.062(4)	Mn_A/Co_A – O(1)	1 × 2.596(4)
Mn_A/Co_A – O(1)	1 × 2.728(5)	Mn_A/Co_A – O(2)	1 × 2.135(4)
Mn_A/Co_A – O(2)	1 × 2.612(4)	Mn_A/Co_A – O(2)	1 × 2.634(5)
Mn_A/Co_A – O(3)	1 × 2.117(3)	Mn_A/Co_A – O(3)	1 × 2.171(3)
Co_B/Mn_B – O(1)	2 × 2.130(1)	Re_B – O(1)	2 × 1.916(1)
Co_B/Mn_B – O(2)	2 × 2.013(1)	Re_B – O(2)	2 × 1.949(1)
Co_B/Mn_B – O(3)	2 × 2.132(2)	Re_B – O(3)	2 × 1.952(2)
Angle	**(°)**	**Angle**	**(°)**
Co_B/Mn_B – O(1) – Re_B	135.3(1)	Co_B/Mn_B – O(3) – Re_B	138.14(7)
Co_B/Mn_B – O(2) – Re_B	141.7(1)		

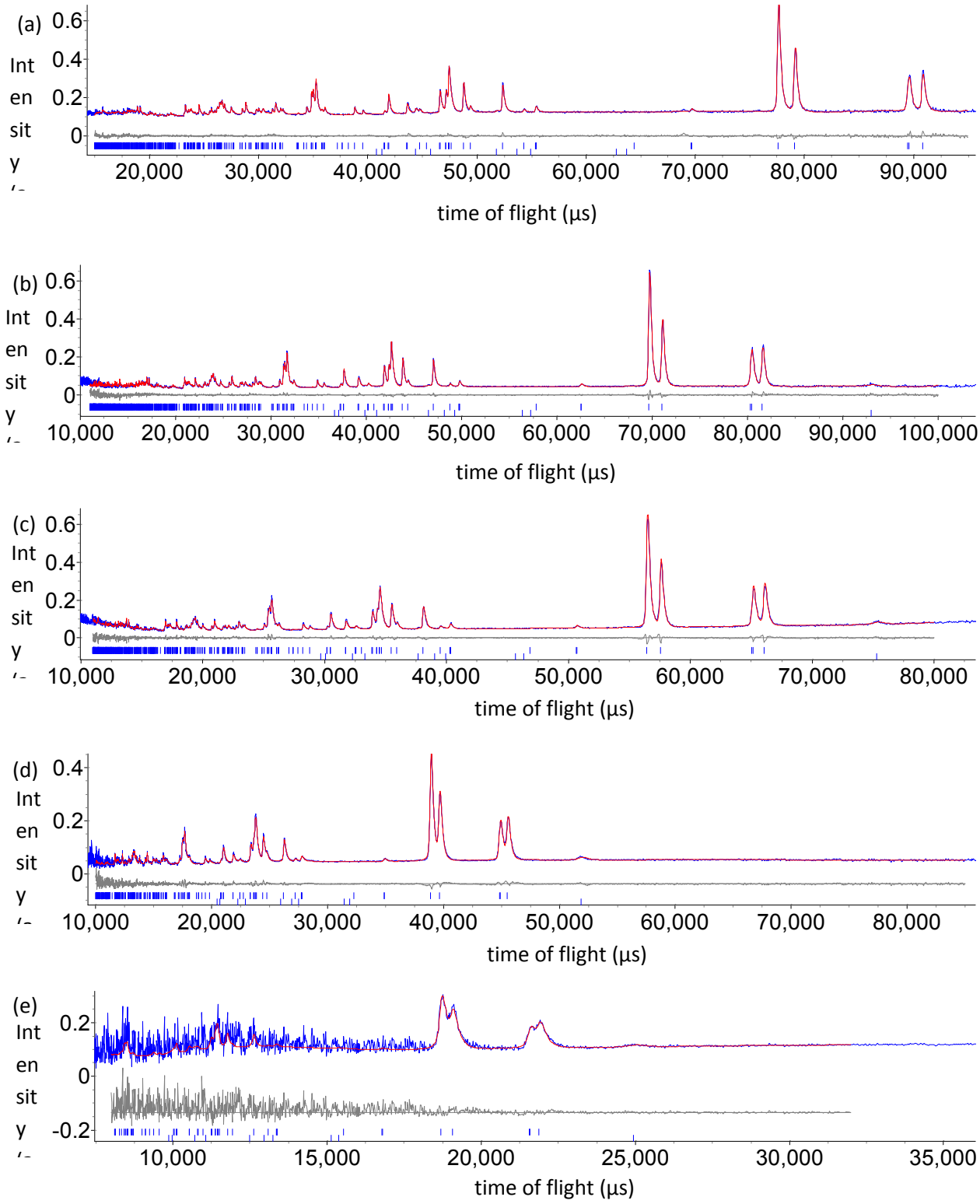

Figure ESI4.1 Refinement profiles for Mn_2CoReO_6 using 200 K NPD data in space group $P2_1/n$ showing (a) higher resolution (153° bank) data, (b) 122° bank data, (c) 90° bank data, (d) 58° bank data and (e) 27° bank data. Observed, calculated and difference profiles are shown in blue, red and grey, respectively; upper and lower blue ticks show reflection positions for the main phase Mn_2FeRuO_6 and for $Mn_{3-x}Co_xO_4$ (fitted with Pawley phase), respectively.

5) Synchrotron Powder X-ray Diffraction

SPXD data were used to confirm the average nuclear structure. In order to measure the sample in an air-and-moisture free environment, a ground sample of Mn_2CoReO_6 crystals were sealed in a quartz ampule, the thickness of which necessitated measurement at the high-energy beamline, 11-ID-C at ANL (λ = 0.1173 Å). The sample refined as 98.79% pure with space group $P2_1/n$ using GSAS-II software[38] (Figure ESI 5.1), and so the trace impurities were not refined in this case. Rietveld Refinement indicates the ordering between Co and Re B and B' cations to be nearly complete, with a *B/B'* antisite disorder of approximately 1.55%, which is in agreement with the SCD results (1.65%). The refined unit cell parameters are close to the those from SCD and NPD refinements. Refinement details and bond lengths are reported in tables ESI5. 1 and 2.

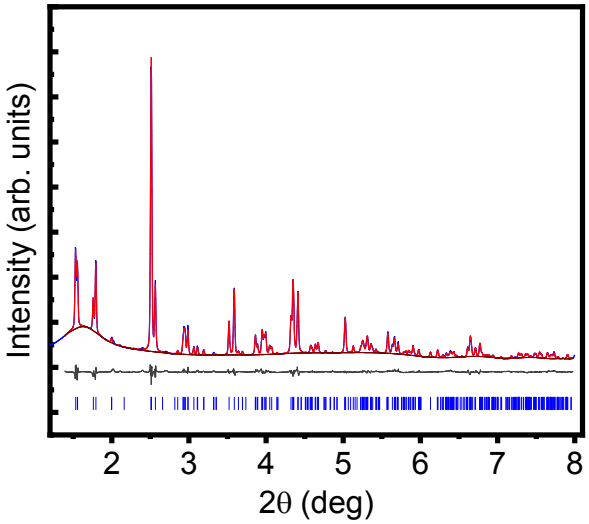

Figure ESI5.1 Refinement profiles for Mn_2CoReO_6 using room temperature SPXD data in space group $P2_1/n$. The observed pattern, calculated pattern, different, and background are shown in light blue, bright red, grey, and deep red lines, respectively. The Bragg positions of Mn_2CoReO_6 are shown as blue ticks.

Table ESI5.1. Selected Bond Distances (Å) for Mn_2CoReO_6 at room temperature collected on high energy beamline 11-ID-C.

MnO_8		CoO_6		
Mn - O1	2.5970 Å	Co	-O1 x2	2.0839 Å
	2.0708 Å		-O2 x2	2.1998 Å
	2.6734 Å		-O3 x2	2. 0690Å
-O2	2.5528 Å	<Co-O>		2.1176 Å
	2.1098 Å			
	2.8108 Å			
-O3	2.1940 Å	ReO_6		
	2.2080 Å	Re	-O1 x2	1.9096 Å
<Mn-O>	2.4021 Å		-O2 x2	1.8504 Å
			-O3 x2	1.9274 Å
		<Re-O>		1.8958 Å

Table ESI5.2 Select details of the SPXD refinement.

Empirical Formula	Mn_2CoReO_6
Formula Weight	451.01 g/mol
Wavelength	0.1173 Å
Crystal System	Monoclinic
Space group	$P2_1/n$ (14)
Unit cell dimensions	a = 5.24037 Å
	b = 5.35787 Å
	c = 7.63610 Å
	α = ϒ = 90 °
	β = 89.9143°.
Volume	214.40017 $Å^3$
Z	2
Reflections collected	2115
Independent reflections	370
Weight R (all data)	wR = 3.185%
R indices (phase)	RF^2: 4.520% , RF: 3.715%
Phase Fraction	98.7851%

6) X-ray Absorption Near-Edge Spectroscopy (XANES)

Mn and Co K-edges: X-ray absorption near edge spectroscopy (XANES) measurements of the K-edges of 3d row transition metals in compounds has proven to be a useful probe of the transition metal valence/configuration.[39-43] These edges are dominated by peak-like 1s to 4p transitions and typically exhibit a chemical shift to higher energies with increasing transition metal valance. This valence/chemical-shift coupling is well illustrated by the shift to higher energy of the centrum of the rising portion of the Mn-K edges in Fig. ESI6.1(right) for the octahedrally coordinated standard spectra sequence $Mn^{2+}O$ to $LaMn^{3+}O_3$ to $CaMn^{4+}O_3$. Indeed, their chemical shifts indicate a Mn^{2+} state for the Mn_2FeReO_6 and $Mn_2Fe_{0.8}Mo_{1.2}O_6$ standards despite their effectively reduced 8-fold (reduced from the un-distorted perovskite-*A*-site 12-fold) value. The Mn K-edge spectrum for Mn_2CoReO_6 exhibits a chemical shift consistent with a Mn^{2+} assignment. In fact, the almost overlapping Mn_2CoReO_6 and Mn_2CoReO_6 spectra also strongly supports a very similar local coordination environment.

The Mn pre-edge (indicated in Fig. ESI6.2 (left)) involves transitions quadrupole and d/p-hybridization induced transitions final d-states.[17, 18] Again, an increasing-valence/chemical-shift-to-higher-energy is typically seen in the pre-edge spectral features, along with changes in the spectral distribution. Comparison of the Mn_2CoReO_6 pre-edge feature to those of the standard compounds further supports the Mn^{2+} assignment for this compound. Thus, both the pre-edge and main-edge Mn K results support a Mn^{2+} state for Mn_2CoReO_6 with the main-edge results also strongly supporting a local coordination environment like that of Mn_2FeReO_6.

Figure ESI6.1 (right) shows the Co-K main edge spectra for Mn_2CoReO_6 compared with several standards in which Co is octahedrally coordinated to oxygen: Co^0, $Co^{2+}O$, $La_2Co^{2+}VO_6$, $LaCo^{3+}O_3$, and $SrCo^{4+}O_{3-\delta}$. The chemical shift of the main edge spectra is consistent with the assignment of an oxidation state of Co(II). Likewise, the energy shift and overall shape of the Co pre-edge of Mn_2CoReO_6 (ESI6.2 (right)) correspond to those of the Co^{2+} standards.

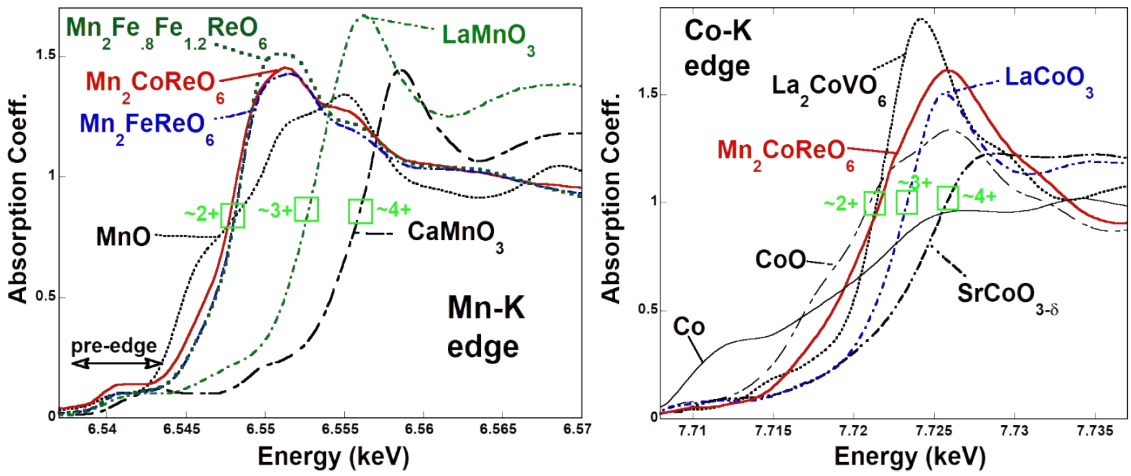

Figure ESI6.1 (left) The Mn-K main edge of Mn_2CoReO_6 compared to those of a series of standard compounds: elemental Mn; octahedrally coordinated $Mn^{2+}O$, $LaMn^{3+}O_3$, and $CaMn^{4+}O_3$; and the $Mn^{2+}{}_2FeReO_6$ and $Mn^{2+}{}_2Fe_{0.8}Mo_{1.2}O_6$ compounds are effectively eight-fold coordinated. Here the green squares have been included to indicate the nominal centrum of the steeply rising main edge that provides a valence state indicator. Note that the pre-edge region, which will be expanded upon in the SI, is also indicated in the figure. (right) The Co-K main edge of Mn_2CoReO_6 compared to those of a series of standard compounds: elemental Co; the octahedrally coordinated $Co^{2+}O$, $La_2Co^{2+}VO_6$, and $LaCo^{3+}O_3$, $LaCo^{\sim 4+}O_{3-\delta}$. Again the green squares have been included to indicate the nominal centrum of the steeply rising main edge that provides a valence state indicator.

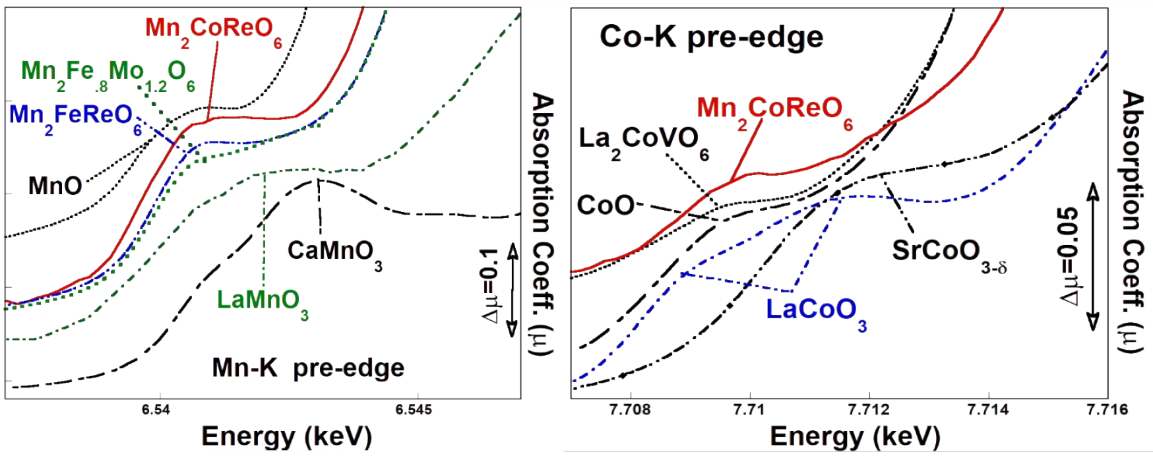

Figure ESI6.2 (left) The Mn-K pre-edge of Mn_2CoReO_6 compared to those of a series of standard compounds: elemental Mn; octahedrally coordinated the $Mn^{2+}O$, $LaMn^{3+}O_3$, and $CaMn^{4+}O_3$; and the $Mn^{2+}{}_2FeReO_6$ and $Mn^{2+}{}_2Fe_{0.8}Mo_{1.2}O_6$ compounds are eight-fold coordinated. Note the low energy chemical shift (and single spectral feature) of the Mn_2CoReO_6 pre-edge supports the Mn^{2+} assignment for this compound. (right) The Co-K pre-edge of Mn_2CoReO_6 compared to those of a series of standard compounds: elemental Co; the octahedrally coordinated $Co^{2+}O$, $La_2Co^{2+}VO_6$, $LaCo^{3+}O_3$; and $LaCo^{\sim 4+}O_{3-\delta}$. Note that the low energy of the pre-edge feature and its spectral distribution support the Co^{2+} assignment for this compound.

Re-$L_{3,2}$ edges: The $L_{2,3}$ near-edges of transition metals manifest intense atomic-like p to d transitions often referred to as white line (WL) features for historical reasons .[18, 43, 44] In octahedrally coordinated Re, the 5d orbitals spilt into lower lying 6-fold-degernate t_{2g} and higher energy 4-fold-degerate e_g orbital states. In Figure 4 transitions into these split t_{2g}/e_g final states can be seen to yield a bimodal A/B WL-feature in the 5d-$L_{3,2}$ edge spectra. Here the A and B feature intensities are respectively related the number of available t_{2g} and e_g final states (hole count) weighted by transition matrix element affects. In the compounds considered here, the e_g hole count (and the B-feature intensity) remains essentially constant. On the other hand, the intensity of the A-feature (relative to the B-feature) very dramatically decreases as the t_{2g} hole count decreases from six in d^0, $SrFe_{3/4}Re_{1/4}O_3$ to three in d^3, ReO_2. Comparing the L_3-edge, Figure ESI6.2, and L_2-edge, Figure 1 (main text), spectra, it is interesting to note that matrix element affects substantially enhance the A-feature intensity (and its change with hole count) especially in the high hole count regime. Thus, the relative A/B feature intensities provides direct insight into the Re valence/d electron-configuration. For the purpose of illustrating the A/B intensity variation, with varying d-count, the L_2-edges in Figure 1 (main text) have been shifted in energy so as to roughly align the B- features. In contrast, the L_3-edges in Figure ESI6.3 are plotted on an absolute energy scale (determined via simultaneously run standards) thereby illustrating the chemical shift of the centrum of the WL-feature to higher energy with increasing Re-valence. In both figures, the comparison of the Mn_2CoReO_6 spectra to the systematic series of standards, can be seen to manifest a relative A/B feature intensity consistent with a ~Re^{6+}, d^1 configuration. Here (and throughout) the approximately notation (~) is used to emphasize the implicit nominal approximation when assigning an integral valence/d-configuration in a hybridized solid-state environment. The Re-L_3-edge of Mn_2CoReO_6 (Figure ESI6.3) can be seen to have a chemical shift also quite consistent with a ~Re^{6+}, d^1 configuration. Thus, both the spectral energy distribution and chemical shift concur in the ~Re^{6+}, d^1 configuration assignment for Mn_2CoReO_6.

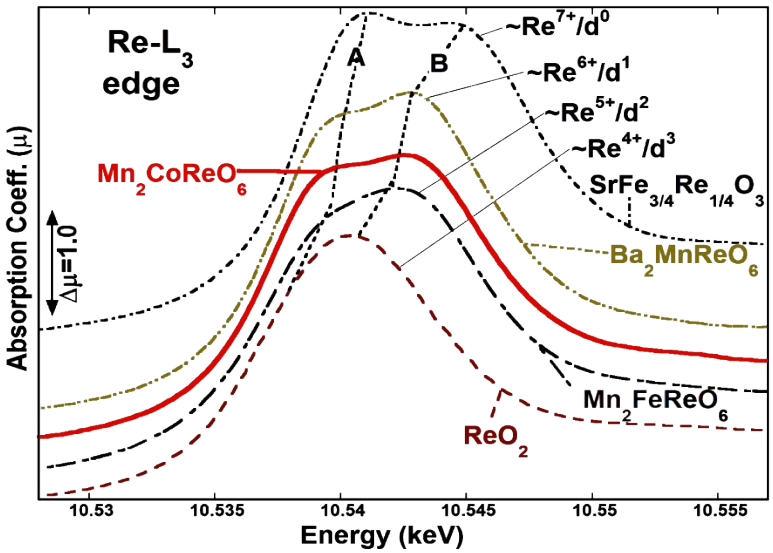

Figure ESI6.3 The Re L_3 edge for Mn_2CoReO_6 compared to those of other standard octahedral Re-O compounds (spanning the Re^{7+}/d^0 - to – Re^{4+}/d^3 configurations). Note that dashed lines have been added to highlight the bimodal A/B structures typical of such 5d transition metal compounds, and that the relative chemical shifts of the spectra are apparent. The spectra have been displaced vertically for clarity.

7) Magnetic properties

The thermal variation of the inverse magnetic susceptibility, χ^{-1}, is also shown in Figure 2 (main text). Fitting χ^{-1} in the temperature range T > 210 K to the Curie-Weiss (CW) form, $\chi^{-1} = (T+\theta)/C$, yields C= 9.76 emu·K mol^{-1} and a "ferromagnetic-like" θ = 25.6 K. This high temperature CW fit is shown as a dotted line in Figure 2 (main text). From the high temperature CW fit the μ_{eff} for Mn_2CoReO_6 is 8.84 μ_B/f.u. as per the following equation:[45]

$$\mu_{eff} = (\frac{3kC}{N})^{1/2} = (8C)^{1/2}\mu_B$$

Within a simple spin-only model, with Mn^{2+} (S =5/2 , μ_{eff} = 5.92 μ_B) and Co^{2+}(S = 3/2, μ_{eff} = 3.87 μ_B), and Re^{6+}(S = 1/2, μ_{eff} = 1.73 μ_B), and the relation[46]:

$$\mu_{eff} = \sqrt{2\mu_B(Mn^{2+})^2 + 1\mu_B(Co^{2+})^2 + 1\mu_B(Re^{6+})^2},$$

one calculates a theoretical μ_{eff} of 9.38 μ_B/fu. This agrees adequately with the fitted experimental 8.84 μ_B/f.u. value, with a slight lowering by spin-orbit coupling of Re^{6+}.

The presence of some ferromagnetic component in the system, despite the robust AFM anomaly near 94 K, is underscored by both the θ = 25.6 K and the downward curvature of the χ^{-1} data away from the CW fit in the 200 K> T > 94 K temperature range. Indeed, the dramatic sharpness of the peak anomaly in in χ(T) is quite enhanced by the FM response above the AFM ordering temperature T_N~ 94K. Discussion of this FM component will be returned to subsequently.

Below the first transition, the FC and ZFC curves diverge sharply, which may suggest competing magnetic interactions. From the graph of χ^{-1} vs. T (Figure 2 (main text)), data above 200 K exhibit Curie-Weiss behavior, albeit with some curvature which is slight in that region, but increases noticeably as the first magnetic transition approaches. This shape could be due to crystal field effects, as suggested by Retuerto et. al. to explain a similar curve observed in Sr_2CoReO_6.[12] The calculated Curie constant, C, is 9.76 emu·K mol^{-1} and the Weiss temperature is approximately 25.6 K, despite the AFM character of the transition at 94 K. A positive Weiss constant is not unheard of in cobalt-containing antiferromagnets, and it could be that spin orbit effects decrease the reliability of Θ to characterize magnetic order.[47, 48]

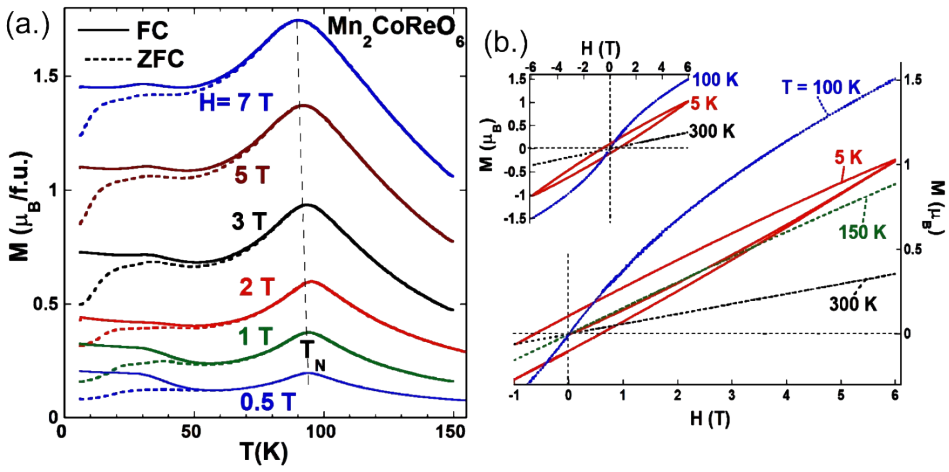

Figure ESI7.1 (a) Magnetization (M) vs temperature for Mn_2CoReO_6 measured at a series of fields (H). The field cooled (FC) and zero field cooled (ZFC) data collection curves are solid and dashed lines respectively. (b) A portion of the magnetization vs field curves, M(H), for Mn_2CoReO_6, measured at temperatures of 5, 100, 150, and 300 K (lower right). Inset (upper left) the full loop M(H) curves at 5, 100 and 300 K to emphasize the field-symmetry of the loops.

Magnetization vs temperature measurements were performed in a series of increasing field strengths up to H= 7 T and are shown in Figure ESI7.1(a). The prominent AFM order induced M(T) peak near 94 K is clearly robust to the highest field studied, and shifts down only slightly in temperature in the higher fields. The robustness of the M(T) signature in field would imply that the field induced reorientation of the AFM order parameter transverse to the external H-field does not occur in this field range. Moreover, magneto-crystalline anisotropy appears strong enough that the applied H-field is unable to induce any significant continuous canting of the AFM order away from its preferred crystalline ordering direction. Discussion of the lower temperature M(T) behavior will be returned to below after discussing selected isothermal magnetization measurements.

The results of selected temperature isothermal magnetization measurements, M(H), are shown in Figure ESI7.1b. The linear behavior of M(H) data at 300 and 150 K are consistent with paramagnetism. However, the S-shaped curve for the M(H) at 100 K, indicates weak FM component. Recall in the discussion of the magnetic susceptibility, shown in Figure 2 (main text), that this is the same temperature range above T_N in which the magnetic susceptibility manifested a FM like curvature away from the CW fit. Moreover, recall also that the CW fit also showed a FM-like Weiss temperature.

Turning to the T = 5 K, M(H) curve shown in Figure ESI7.1(b), one should note several points. Firstly, the magnetization varies smoothly with field with no sign of a field-induced transition. Indeed, even the first leg in which the field is increased from H = 0 to 6T shows a smooth variation. Secondly, the total magnetization at 5 K is only about 1 μ_B (more than an order of magnitude less than the potential 13.5 μ_B /f.u.) consistent with the modest field response within an AFM state. Thirdly, the remnant magnetization, upon decreasing the field has a small ~0.1 μ_B value (and a coercive field of ~0.5 T) consistent with an induced field polarization/modification of the AFM domain structure. Moreover, the entire M(H) loop at 5 K is consistent with such gradual/modest field induced AFM domain structure modifications.

The discussion of the field dependent M(T) behavior below T_N will now be returned to. Specifically, the M(T) curves exhibit structures in the T< 50 K range and the structures are quite different under FC and ZFC data collection. It is possible that some form of spin reorientation transition (or evolution) is active in this temperature range. A change in the Re contribution in the magnetic order is also possible. Such changes are not inconsistent with the temperature dependent neutron scattering results but they are also not clear given the refinement limitations.

However, in view of the T = 5 K M(H) results it would appear that such effects are modest and that a robust AFM state persists in this temperature range. It is also possible that AFM domain effects are responsible for this T< 50 K magnetic behavior. The NPD structural refinement found an ~16% antisite disorder between *A*-site Mn and *B*-site Co. Such interchanging of S= 5/2 and 3/2 at sites allows for a local uncompensated moment that, when coupled to other disorder effects, can enhance the coupling of external magnetic field. Above T_N, AFM fluctuations with modest net magnetic moments would respond to an external field and could motivate the FM components observed in χ^{-1} for $T > T_N$ (see Figure 2 (main text)) and in the M(H) at 100K (see Figure ESI7.1(b)). Similarly, FC conditions would lead to a nucleation and growth of AFM domains with larger net moments aligned with the field, whereas ZFC conditions would lead to a low-magnetization/random-domain growth.

8) Magnetotransport measurements

Additional low field magnetic properties were evaluated in the form of temperature dependent resistivity measurements under applied magnetic fields of 0 T and 7 T, as shown in Figure ESI8.1. The resistance values are almost identical under 300 - 50K, where resistivity becomes too high to accurately measure, which indicates a lack of magnetoresistance. At 300 K, roughly room temperature, the resistivity is approximately 6.98Ω cm and 7.05 Ω cm at 0 T and 7 T, respectively, similar to what was reported for the non-magnetoresistive half-metal Mn_2MnReO_6 at the same temperature (6.80 Ω cm and 8.10 Ω cm at 0 T and 9 T).[18] The temperature dependence of ρ, (Figure ESI8.1, inset) was found by trial-and-error fitting of the relation $(1/T)^p$ with p = 1/2 giving the best linearity from 50 – 300 K. This fitting is consistent with that of an Efros-Shklovskii variable range-hopping semiconductor, ($\rho = \rho_0 \exp(T_0/T)^{1/2}$ where T_0 is the characteristic temperature) in which a 'soft', or parabolic, gap in the density of states near the Fermi level is caused by Coulomb interactions between localized electrons.[49] The extracted values for respectively.

Previously-explored $Mn_2BB'O_6$ compounds (B = Fe, Mn), have presented both giant magnetoresistance an no magnetoresistance.[17, 18] Mn_2FeReO_6, a half-metallic ferrimagnet, demonstrated giant positive magnetoresistance of 220% at 5K due to the magnetically ordered Mn sublattice interfering with Fe-O-Re exchange. Conversely, the *A* and *B-B'* magnetic sublattices in Mn_2MnReO_6 couple antiferromagnetically and hinder the possibility of ferrimagnetic interactions or a half metallic state between Re and Mn, greatly decreasing the probability of magnetoresistance. In Mn_2CoReO_6, the previously shown robust AFM character of the magnetic ordering also indicates a lack of ferrimagnetic interactions after T_N, and so magnetoresistance should not be expected in this case.

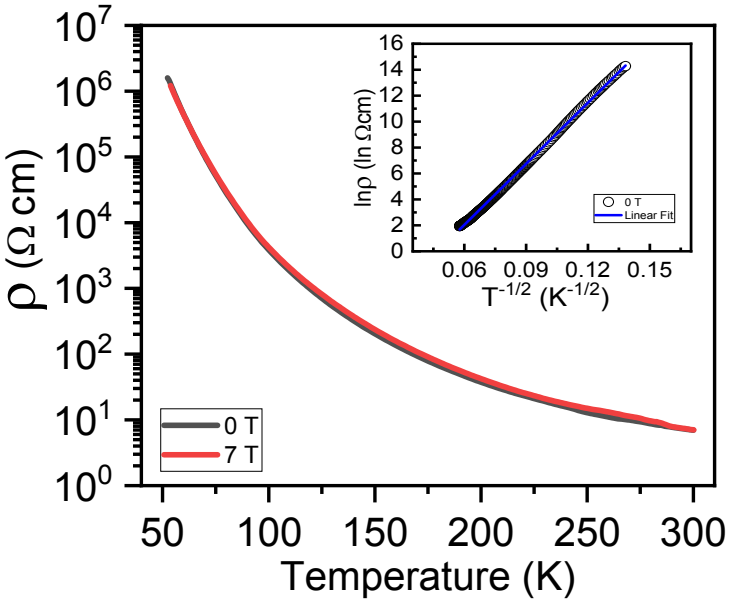

Figure ESI8.1 Mn_2CoReO_6 temperature dependent resistivity, ρ, measured at 0 T and the linear fit plot of ρ versus $T^{-1/2}$ (inset) which indicate an Efros–Shklovskii variable range hopping mechanism.

9) Heat capacity measurements

The specific heat in Figure ESI9.1 very clearly manifests an asymmetric, rounded λ-anomaly peaking very near 96 K that closely corresponds to the sharp transition seen in the magnetic susceptibility at H = 0.5 T (Figure 2 (main text)), confirming that the antiferromagnetic order in Mn_2CoReO_6 occurs at 94 K. Specific heat confirms T_N at ~94 K, as that is the midpoint between the onset of the large irregular anomaly at 108 K and the end of the most dramatic slope change at 81 K. Within material and experimental limits these results confirm the presence of a second order AFM transition in Mn_2CoReO_6 in this temperature range. There may be another transition near 50 K, where the slope changes slightly yet again, and while this corresponds with a change in measurement mode and thus transition shape and exact position could be artificially affected, this latter transition is also observed in the NPD.

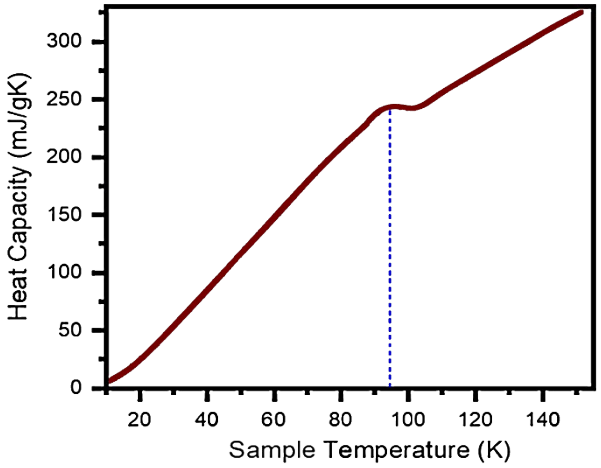

Figure ESI9.1. Specific heat capacity versus temperature for Mn_2CoReO_6 .

10) Magnetic structure from NPD

Table ESI10.1 Nuclear refinement details from Rietveld refinement of Mn_2CoReO_6 using 60 K NPD data in space group $P2_1/n$ with a = 5.2304(1) Å, b = 5.3421(1) Å, c = 7.6293(2) Å, β 89.825(1)°; R_{wp} = 3.56%, R_p = 4.12% and χ^2 = 4.28.

Atom	**site**	***x***	***y***	***z***	**Factional occupancy**	**U_{iso} × 100 (Å²)**
Mn_A/Co_A	4*e*	0.4930(4)	0.5513(4)	0.7460(4)	0.9197(9)/0.0803(9)†	1.19(8)*
Co_B/Mn_B	2*c*	0	0.5	0	0.8394(9)/0.1606(9)†	1.19(8)*
Re_B	2*d*	0.5	0	0	1	0.38(7)
O(1)	4*e*	0.3419(3)	0.3043(4)	0.9296(2)	0.940†	1.12(9)
O(2)	4*e*	0.3106(3)	0.3196(3)	0.5574(2)	0.985†	0.43(8)
O(3)	4*e*	0.8803(2)	0.4333(2)	0.7378(2)	0.965†	0.38(7)

† occupancies fixed at values from 200 K refinement (Table 1)

* constrained to be identical

Table ESI10.2 Magnetic refinement details from Rietveld refinement of Mn_2CoReO_6 using 60 K NPD data in space group $P2_1/n$ with a = 5.2304(1) Å, b = 5.3421(1) Å, c = 7.6293(2) Å, β 89.825(1)°; moments are defined with respect to Cartesian axes.

Atom	**site**	***x* moment (μ_B)**	***y* moment (μ_B)**	***z* moment (μ_B)**	**Total moment (μ_B)**
Mn_A/Co_A	4*e*	1.323(7)	1.156(6)	1.657(9)	2.41(7)
Co_B/Mn_B	2*c*	0	2.41(1)	0	2.41(1)

Re_B	2*d*	0	0.804(6)	0	0.804(6)

Table ESI10.3 Selected bond lengths and angles from Rietveld refinement of Mn_2CoReO_6 using 60 K NPD data in space group $P2_1/n$.

Bond	**Length (Å)**	**Bond**	**Length (Å)**
Mn_A/Co_A – O(1)	1 × 2.079(4)	Mn_A/Co_A – O(1)	1 × 2.589(3)
Mn_A/Co_A – O(1)	1 × 2.734(4)	Mn_A/Co_A – O(2)	1 × 2.126(4)
Mn_A/Co_A – O(2)	1 × 2.610(3)	Mn_A/Co_A – O(2)	1 × 2.622(4)
Mn_A/Co_A – O(3)	1 × 2.122(3)	Mn_A/Co_A – O(3)	1 × 2.149(3)
Co_B/Mn_B – O(1)	2 × 2.139(1)	Re_B – O(1)	2 × 1.902(2)
Co_B/Mn_B – O(2)	2 × 2.021(1)	Re_B – O(2)	2 × 1.940(1)
Co_B/Mn_B – O(3)	2 × 2.128(2)	Re_B – O(3)	2 × 1.950(2)
Angle	**(°)**	**Angle**	**(°)**
Co_B/Mn_B – O(1) – Re_B	135.3(1)	Co_B/Mn_B – O(3) – Re_B	138.53(7)
Co_B/Mn_B – O(2) – Re_B	141.3(1)		

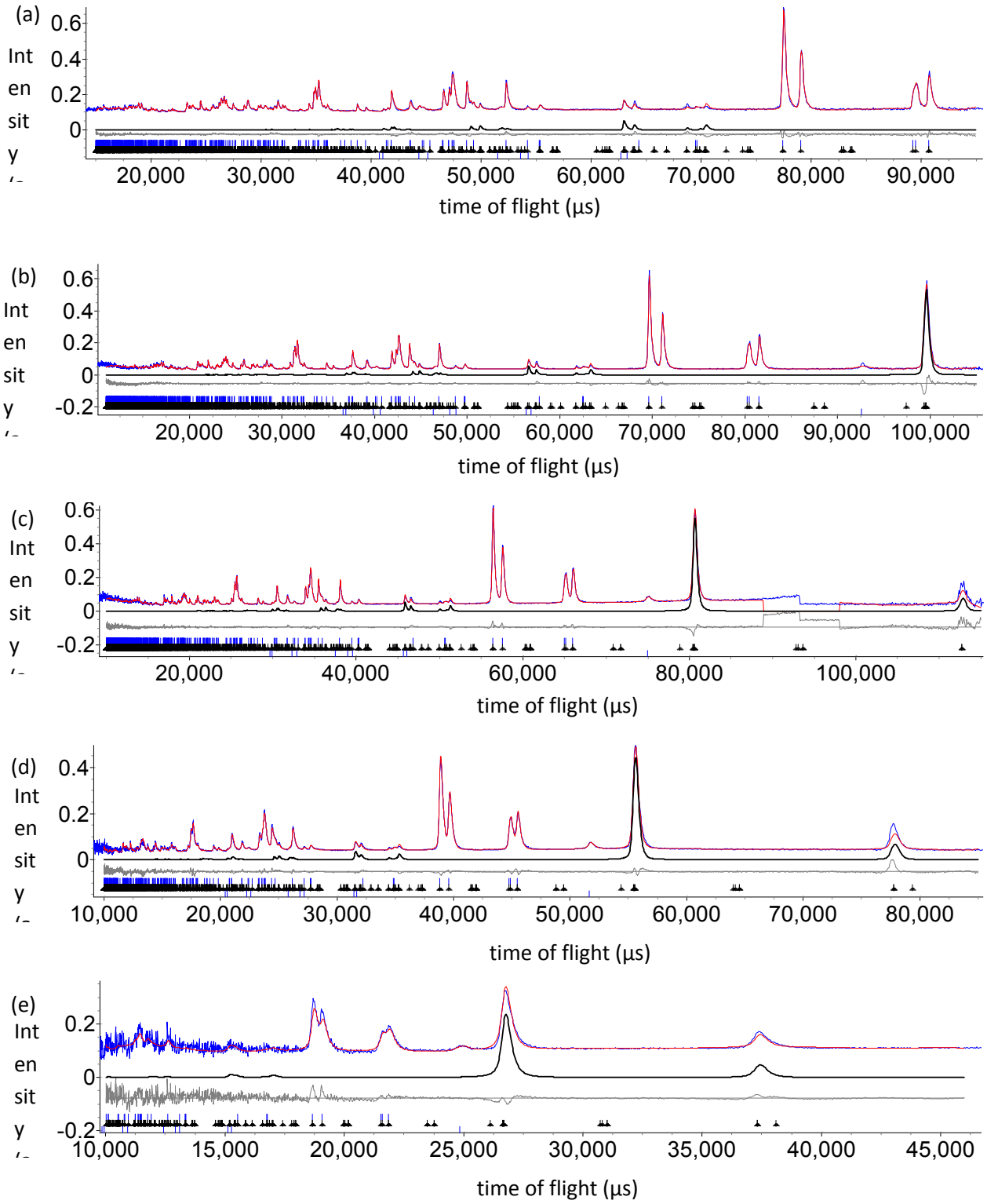

Figure ESI10.1 Refinement profiles for Mn_2CoReO_6 using 60 K NPD data in space group $P2_1/n$ with magnetic scattering highlighted in black for mD1-mD2 magnetic model as described in text showing (a) higher resolution (153° bank) data, (b) 122° bank data, (c) 90° bank data, (d) 58° bank data and (e) 27° bank data. Observed, calculated and difference profiles are shown in blue, red and grey, respectively; upper blue, middle black and lower blue ticks show reflection positions for the main phase Mn_2FeRuO_6, the magnetic phase and for $Mn_{3-x}Co_xO_4$ (fitted with Pawley phase), respectively.

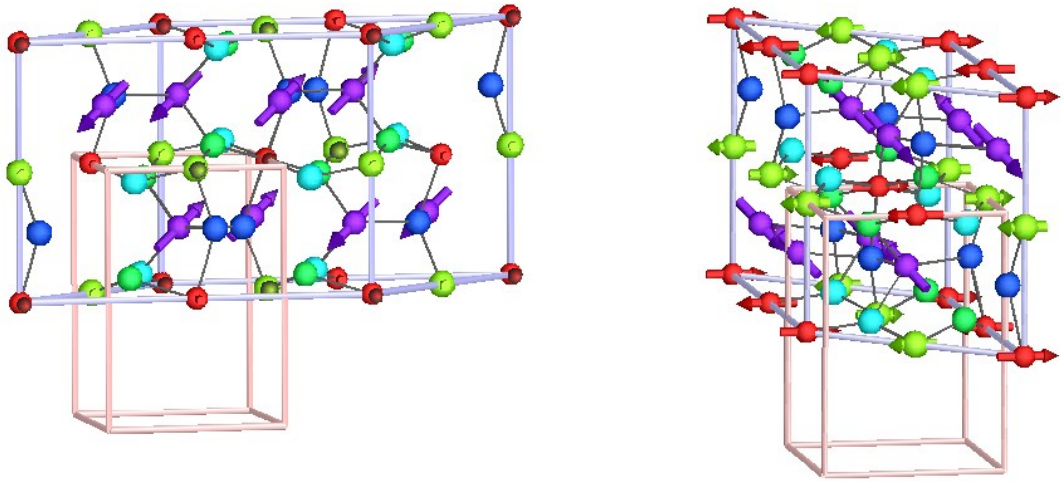

Figure ESI10.2 P_s-1 magnetic unit cell (blue) with basis (-1 1 -1)(-1 1 0)(0 2 0) relative to the nuclear unit cell (pink). Mn_A, Co_B, Re_B and O sites (and moments, as appropriate) are shown in purple, red and green, respectively.

11) Analysis of variable temperature NPD data:

NPD data collected on warming were analyzed using sequential refinements to consider whether magnetic phase transitions occurred below T_N. Initially, the magnetic Bragg scattering was fitted by a Pawley phase and the intensities of magnetic Bragg reflections are shown below. The sum of the magnetic scattering increases smoothly on cooling below 100 K. However, some very weak reflections are only observed on cooling well below T_N, suggesting that there may be changes in the magnetic structure below T_N, perhaps analogous to those reported for Mn_2MnReO_6 or Mn_2FeReO_6.[17-19, 35] This is hard to understand in the light of the single phase transition evident from heat capacity measurements and may suggest some phase separation on cooling; further investigation of the low temperature magnetic behavior is ongoing.

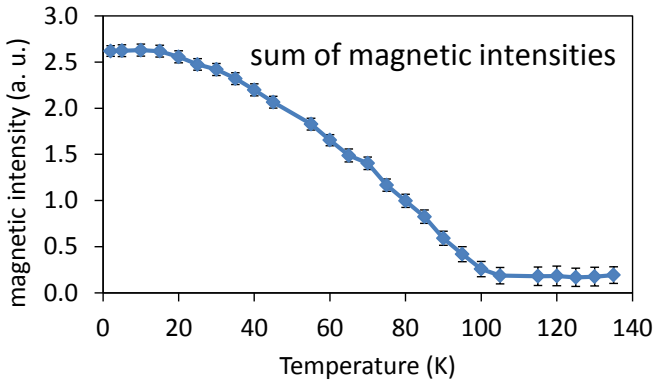
sum of magnetic intensities
magnetic intensity (a. u.)
Temperature (K)

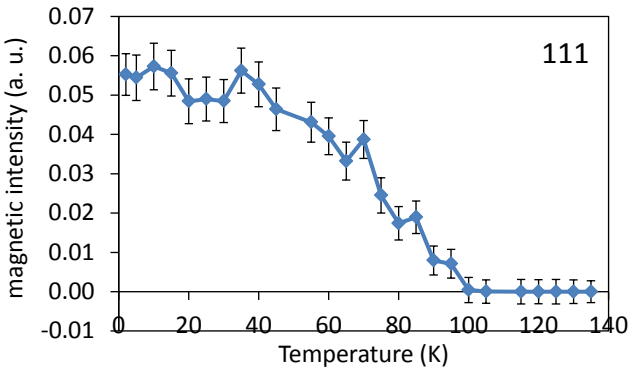
111
magnetic intensity (a. u.)
Temperature (K)

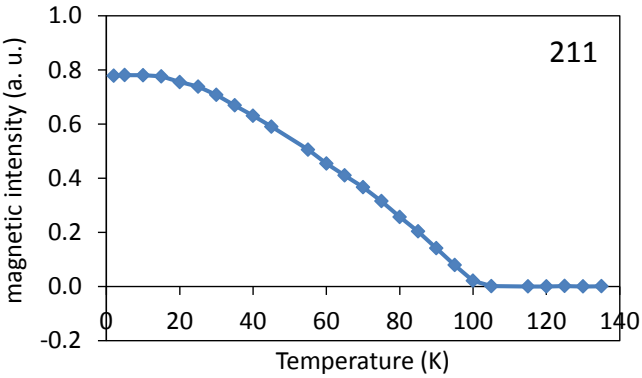
211
magnetic intensity (a. u.)
Temperature (K)

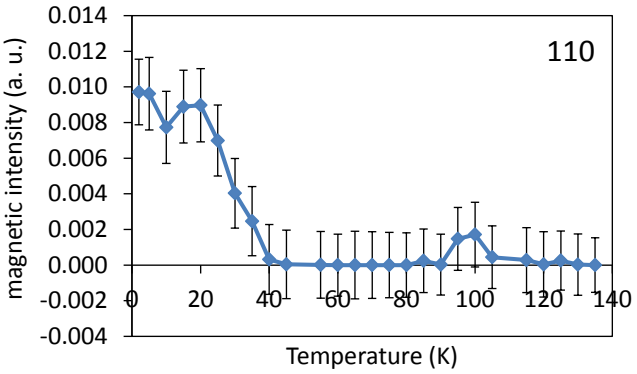
110
magnetic intensity (a. u.)
Temperature (K)

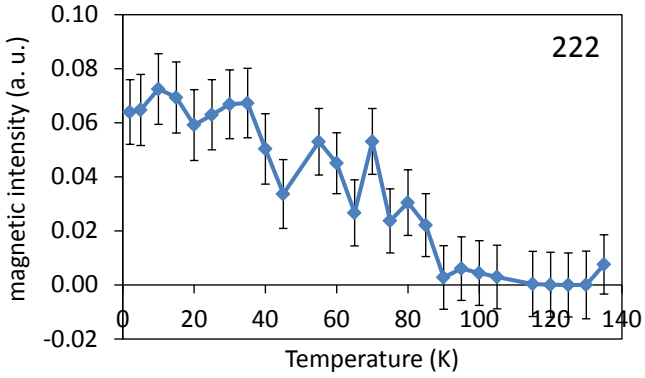
222
magnetic intensity (a. u.)
Temperature (K)

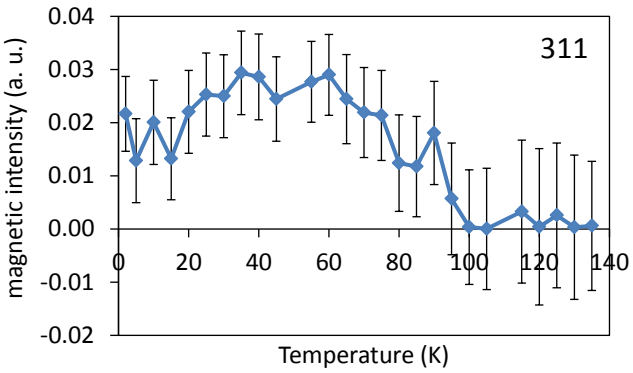
311
magnetic intensity (a. u.)
Temperature (K)

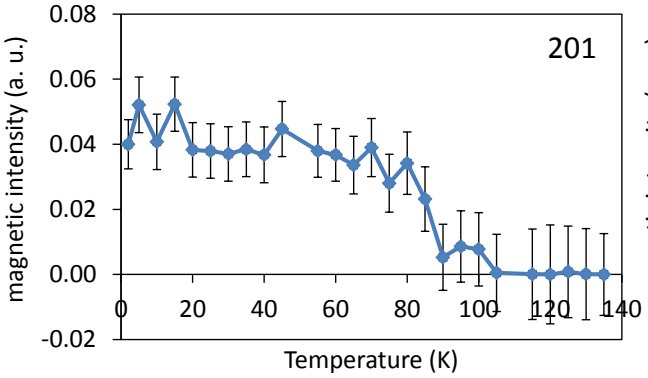
201
magnetic intensity (a. u.)
Temperature (K)

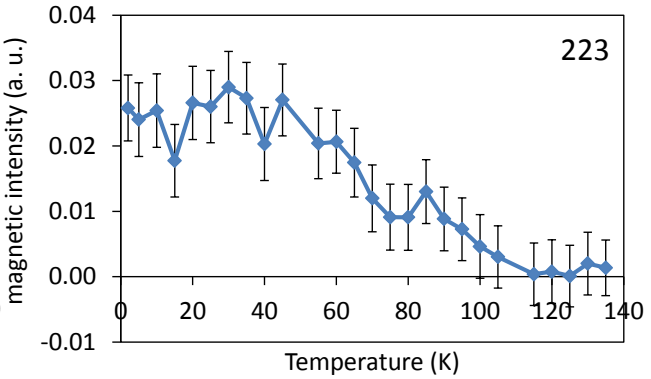
223
magnetic intensity (a. u.)
Temperature (K)

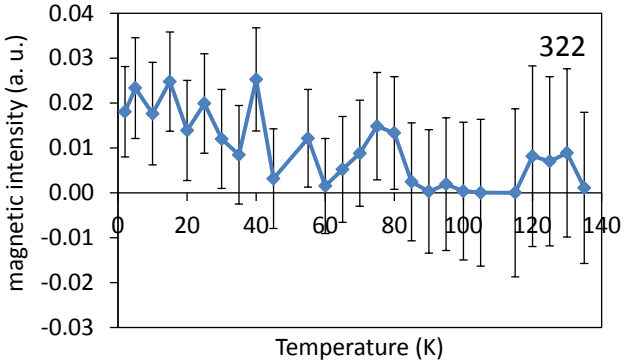
322
magnetic intensity (a. u.)
Temperature (K)

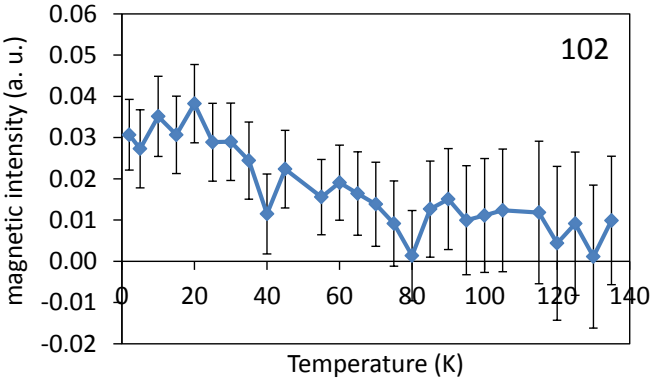
102
magnetic intensity (a. u.)
Temperature (K)

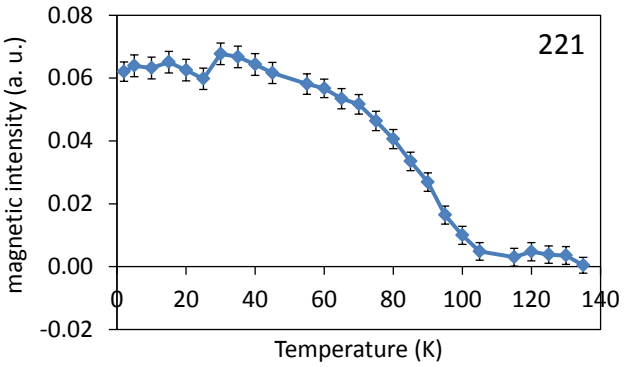
221
magnetic intensity (a. u.)
Temperature (K)

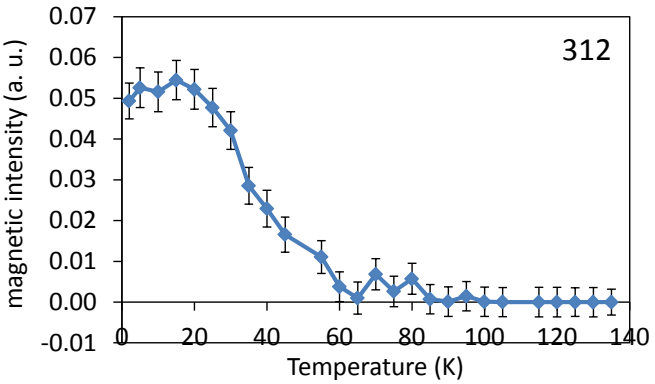
312
magnetic intensity (a. u.)
Temperature (K)

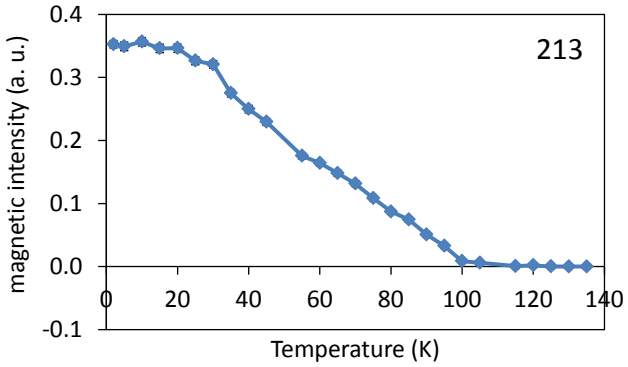
213
magnetic intensity (a. u.)
Temperature (K)

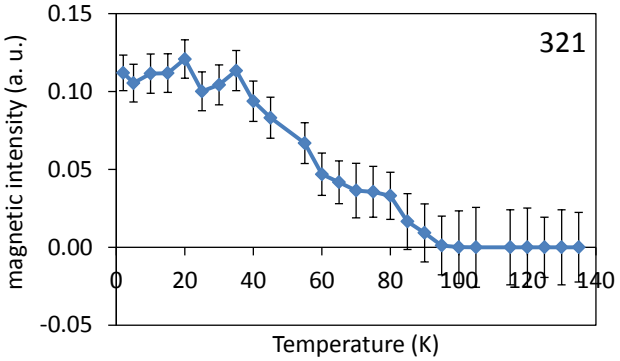
321
magnetic intensity (a. u.)
Temperature (K)

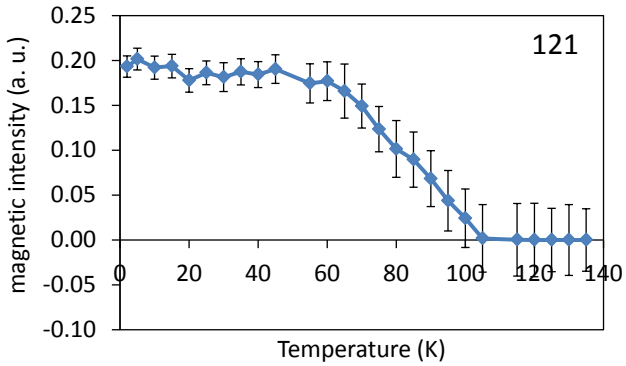
121
magnetic intensity (a. u.)
Temperature (K)

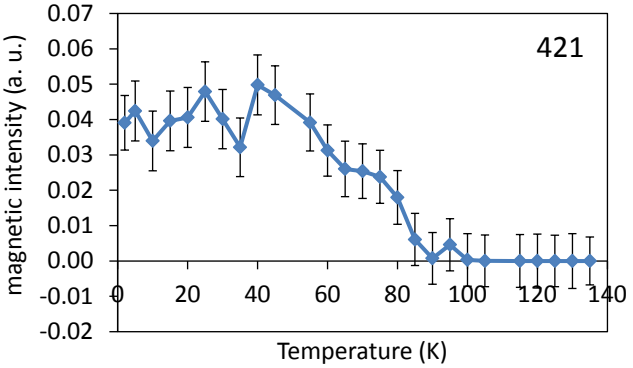
421
magnetic intensity (a. u.)
Temperature (K)

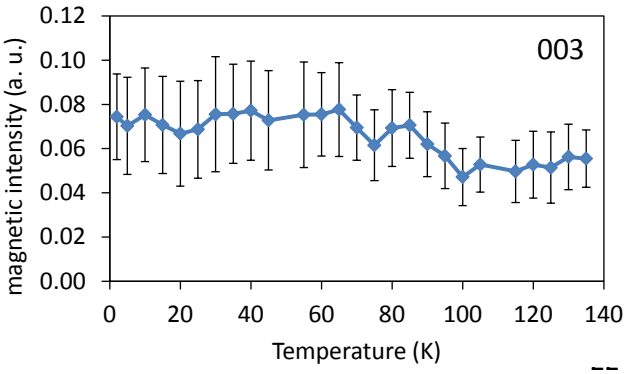
003
magnetic intensity (a. u.)
Temperature (K)

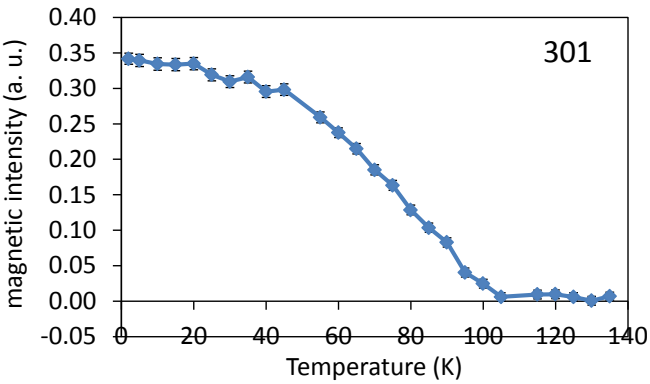
301
magnetic intensity (a. u.)
Temperature (K)

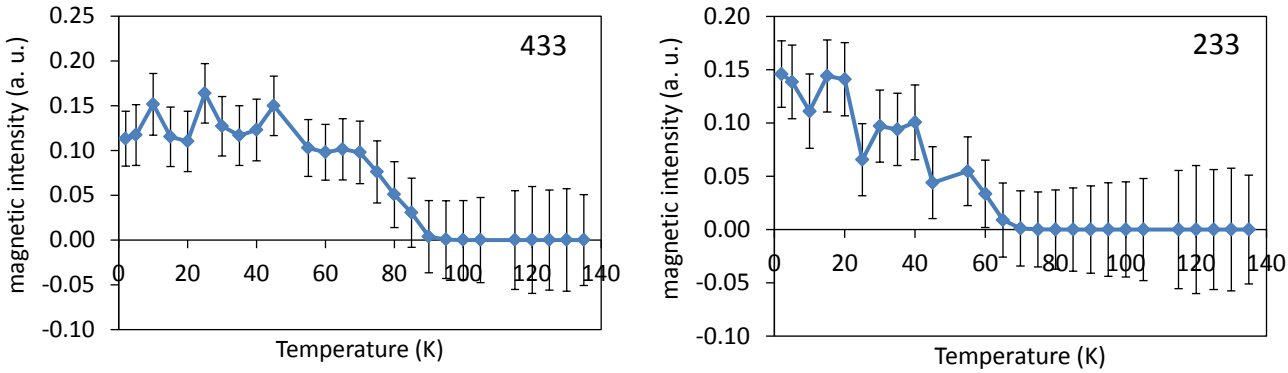

Figure ESI11.1 Results from sequential refinements using bank 3 (90° bank) NPD data. The nuclear phase was fitted by a Rietveld phase, whilst the magnetic Bragg scattering was fitted using a Pawley phase of P_s-1 symmetry with basis (-1 1 -1)(-1 1 0)(0 2 0) relative to the nuclear unit cell (illustrated below).

Sequential Rietveld refinements were also carried out to follow the evolution of the nuclear and magnetic structures on cooling and the trends in lattice parameters and overall magnetic moments with temperature are shown in Figure ESI11.2 below.

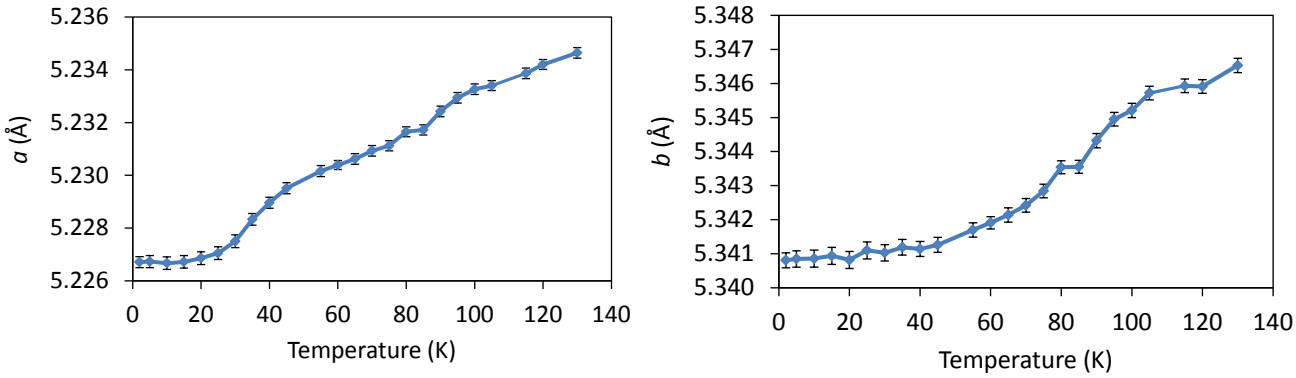

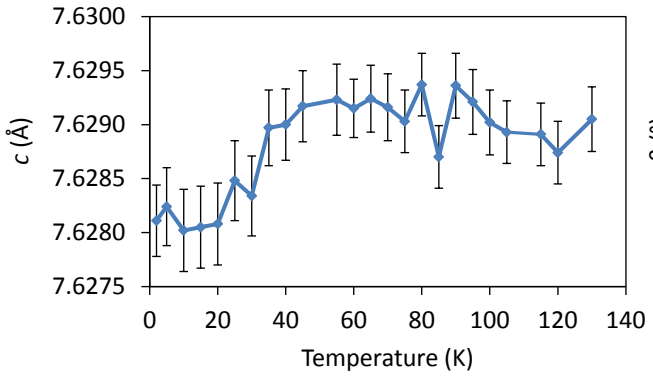
c (Å)
7.6300
7.6295
7.6290
7.6285
7.6280
7.6275
0 20 40 60 80 100 120 140
Temperature (K)

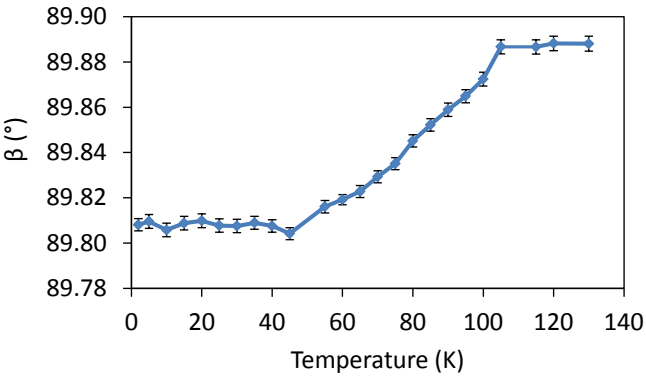
β (°)
89.90
89.88
89.86
89.84
89.82
89.80
89.78
0 20 40 60 80 100 120 140
Temperature (K)

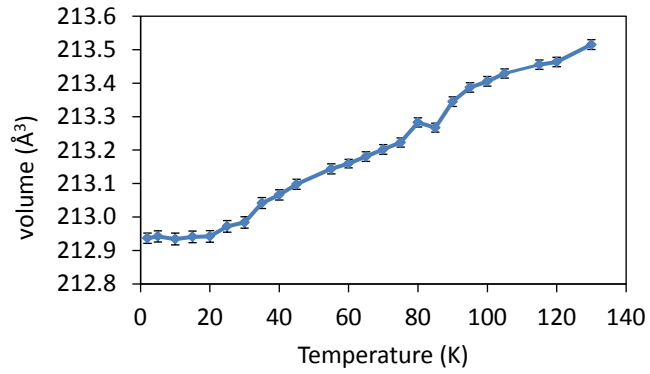
volume (Å³)
213.6
213.5
213.4
213.3
213.2
213.1
213.0
212.9
212.8
0 20 40 60 80 100 120 140
Temperature (K)

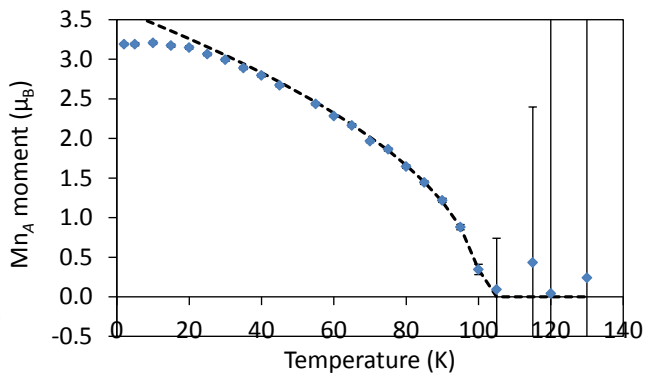
Mn_A moment (μ_B)
3.5
3.0
2.5
2.0
1.5
1.0
0.5
0.0
-0.5
0 20 40 60 80 100 120 140
Temperature (K)

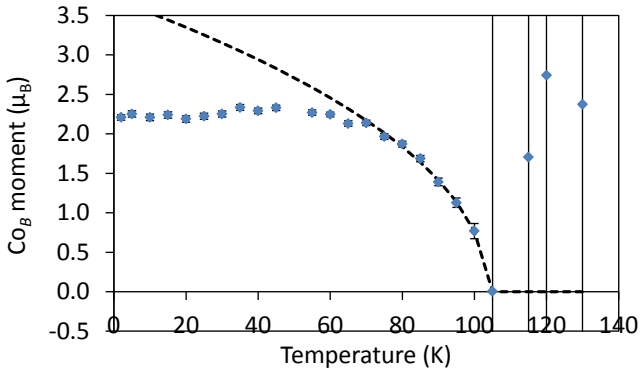
Co_B moment (μ_B)
3.5
3.0
2.5
2.0
1.5
1.0
0.5
0.0
-0.5
0 20 40 60 80 100 120 140
Temperature (K)

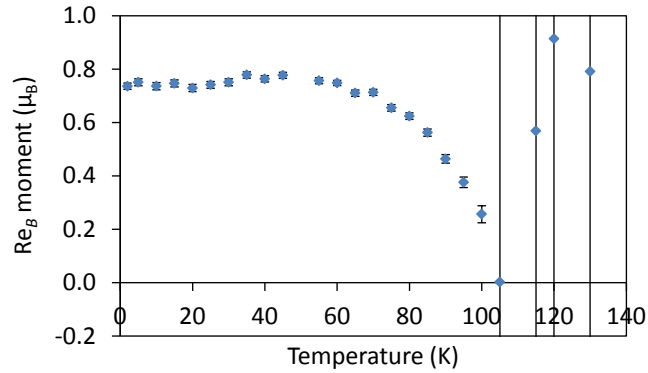
Re_B moment (μ_B)
1.0
0.8
0.6
0.4
0.2
0.0
-0.2
0 20 40 60 80 100 120 140
Temperature (K)

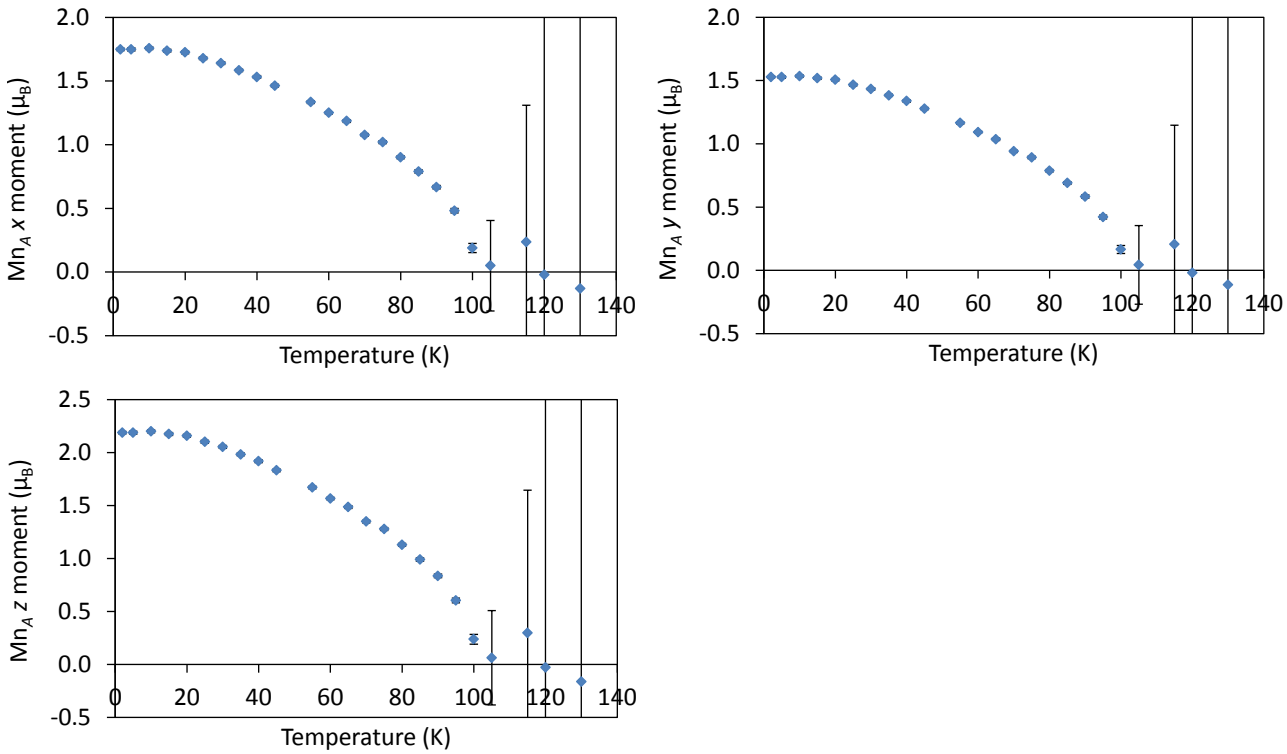

Figure ESI11.2 Trends in lattice parameters and total moments per site with temperature for Mn_2CoReO_6 from sequential refinements using 90° bank NPD data; Rietveld phases were used to fit the nuclear and magnetic structures (with constraints to keep the magnetic unit cell commensurate with the nuclear unit cell) and Bragg scattering from the spinel phase fitted by a Pawley phase. Experimental values for the magnetic moments per site are shown by solid points, but for Co and Mn, a dashed line gives a guide to the eye for a fit to critical behavior: for Mn $M_T = M_0\left(1 - \frac{T}{T_N}\right)^{\beta}$ with $M_0 = 3.6(3)$ μB, $T_N = 100.9(4)$ K and $\beta = 0.50(5)$; for Co $M_T = M_0\left(1 - \frac{T}{T_N}\right)^{\beta}$ with $M_0 = 3.7(2)$ μB, $T_N = 104(1)$ K and $\beta = 0.48(5)$.

12) Fit and Comparison of 2 K NPD Data:

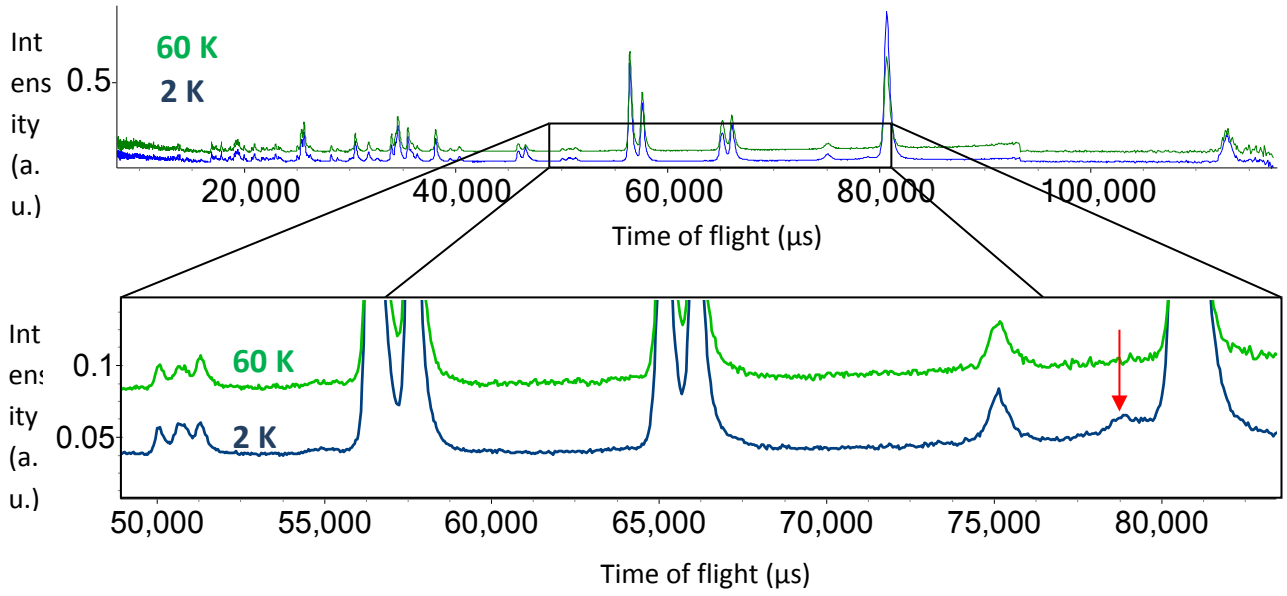

Figure ESI12 90° bank data collected at 60 K (green, upper) and at 2 K (blue, lower) showing additional gamma point reflection (110 of the nuclear unit cell) at 2 K highlighted by arrow. No intensity is predicted for this reflection with our 60 K magnetic model.

While there are some uncertainties in the long-rang magnetic order at 2 K, fitting the 90° bank data collected at low temperature (Figure ESI12, blue) reveals an additional gamma point reflection. This weak reflection corresponds to 110 in the nuclear unit cell, and is not predicted to have intensity with the 60 K magnetic model (seen here in green). This could be further evidence of the additional 40 K magnetic transition, as suggested by both specific heat measurements and by the FM-like feature seen in the magnetic susceptibility measurements. Further experimentation, such as NPD collected at smaller temperature intervals, would be required to determine the nature of the 40 K anomaly with full confidence.

12) References:

1. K. I. Kobayashi, T. Kimura, H. Sawada, K. Terakura and Y. Tokura, *Nature*, 1998, **395**, 677.
2. W. H. Baur, W. Joswig, G. Pieper and D. Kassner, *J. Solid State Chem.*, 1992, **99**, 207-211.
3. M. Retuerto, F. Jiménez-Villacorta, M. J. Martínez-Lope, Y. Huttel, E. Roman, M. T. Fernández-Díaz and J. A. Alonso, *Phys. Chem. Chem. Phys.*, 2010, **12**, 13616-13625.
4. A. K. Paul, M. Jansen, B. Yan, C. Felser, M. Reehuis and P. M. Abdala, *Inorg. Chem.*, 2013, **52**, 6713-6719.
5. J. S. Park, B. J. Han, C. S. Kim and B. W. Lee, *J. Magn. Magn. Mater.*, 2001, **226-230**, 741-742.
6. K. I. Kobayashi, T. Kimura, Y. Tomioka, H. Sawada, K. Terakura and Y. Tokura, *Phys. Rev. B* 1999, **59**, 11159-11162.
7. D. D. Sarma, P. Mahadevan, T. Saha-Dasgupta, S. Ray and A. Kumar, *Phys. Rev. Lett.*, 2000, **85**, 2549-2552.

8. S. E. Lofland, T. Scabarozi, Y. Moritomo and S. Xu, *J. Magn. Magn. Mater.*, 2003, **260**, 181-183.
9. M. T. Anderson, K. B. Greenwood, G. A. Taylor and K. R. Poeppelmeier, *Progress in Solid State Chemistry*, 1993, **22**, 197-233.
10. M. Musa Saad H.-E and N. Rammeh, *Solid State Communications*, 2016, **248**, 129-133.
11. M. Retuerto, M.-R. Li, P. W. Stephens, J. Sánchez-Benítez, X. Deng, G. Kotliar, M. C. Croft, A. Ignatov, D. Walker and M. Greenblatt, *Chem. Mater.*, 2015, **27**, 4450-4458.
12. M. Retuerto, M. J. Martínez-Lope, M. García-Hernández, M. T. Fernández-Díaz and J. A. Alonso, *Eur. J. Inorg. Chem.*, 2008, **2008**, 588-595.
13. S. Vasala and M. Karppinen, *Prog. Solid State Chem.*, 2015, **43**, 1-36.
14. M. W. Lufaso and P. M. Woodward, *Acta Crystallogr. B*, 2001, **57**, 725-738.
15. A. A. Belik and W. Yi, *J. Phys. Condens. Matter*, 2014, **26**, 163201.
16. M. Retuerto, S. Skiadopoulou, F. Borodavka, C. Kadlec, F. Kadlec, J. Prokleška, Z. Deng, J. A. Alonso, M. T. Fernandez-Diaz, F. O. Saouma, J. I. Jang, D. Legut, S. Kamba and M. Greenblatt, *Phys. Rev. B*, 2018, **97**, 144418.
17. M. R. Li, M. Retuerto, Z. Deng, P. W. Stephens, M. Croft, Q. Huang, H. Wu, X. Deng, G. Kotliar, J. Sánchez‐Benítez, J. Hadermann, D. Walker and M. Greenblatt, *Angew. Chem. Int. Ed. Engl.*, 2015, **54**, 12069-12073.
18. Man-Rong Li, Jason P. Hodges, Maria Retuerto, Zheng Deng, Peter W. Stephens, Mark C. Croft, Xiaoyu Deng, Gabriel Kotliar, Javier Sánchez-Benítez, David Walker and M. Greenblatt, *Chemistry of Materials*, 2016, **28**, 3148-3158.
19. A. M. Arévalo-López, F. Stegemann and J. P. Attfield, *Chemical Communications*, 2016, **52**, 5558-5560.
20. A. M. Arevalo-Lopez, G. M. McNally and J. P. Attfield, *Angew. Chem. Int. Ed. Engl.*, 2015, **54**, 12074-12077.
21. G. V. Bazuev, B. G. Golovkin, N. V. Lukin, N. I. Kadyrova and Y. G. Zainulin, *Journal of Solid State Chemistry*, 1996, **124**, 333-337.
22. O. Fukunaga and T. Fujita, *Journal of Solid State Chemistry*, 1973, **8**, 331-338.
23. M.-R. Li, P. W. Stephens, M. Croft, Z. Deng, W. Li, C. Jin, M. Retuerto, J. P. Hodges, C. E. Frank, M. Wu, D. Walker and M. Greenblatt, *Chem. Mater.*, 2018, **30**, 4508-4514.
24. M.-R. Li, M. Retuerto, D. Walker, T. Sarkar, P. W. Stephens, S. Mukherjee, T. S. Dasgupta, J. P. Hodges, M. Croft, C. P. Grams, J. Hemberger, J. Sánchez-Benítez, A. Huq, F. O. Saouma, J. I. Jang and M. Greenblatt, *Angew. Chem. Int. Ed*, 2014, **53**, 10774-10778.
25. *APEX3*, **version 2015.9‐0; Bruker AXS: Madison, WI, 2015.**
26. *SAINT*, version 8.34A; Bruker AXS: Madison, WI, 2013.
27. G. M. Sheldrick, *SHELXT‐2014/5*, University of Göttingen: Göttingen, Germany, 2014.
28. G. M. Sheldrick, *Acta Crystallographica*, 2015, 3-8.
29. A. A. Coelho, *TopasAcademic Software*, 2012, **5th edition**.
30. B. J. Campbell, H. T. Stokes, D. E. Tanner and D. M. Hatch, *J. Appl. Cryst.*, 2006, **39**, 607-614.
31. C. J. Howard, B. J. Kennedy and P. M. Woodward, *Acta Crystallographica Section B*, 2003, **B59**, 463-471.
32. K. Momma and F. Izumi, *Journal of Applied Crystallography*, 2011, **44**, 1272-1276.
33. M. Scimeca, S. Bischetti, H. K. Lamsira, R. Bonfiglio and E. Bonanno, *European journal of histochemistry : EJH*, 2018, **62**, 2841-2841.
34. B. M. Alsmadi and P. Fox, *Colloids and Surfaces A: Physicochemical and Engineering Aspects*, 2001, **194**, 249-261.
35. Q. Zhou, P. J. Saines, N. Sharma, J. Ting, B. J. Kennedy, Z. Zhang, R. L. Withers and K. S. Wallwork, *Chem. Mater.*, 2008, **20**, 6666-6676.
36. Z. Zhang, C. J. Howard, B. J. Kennedy, K. S. Knight and Q. Zhou, *J. Solid State Chem.*, 2007, **180**, 1846-1851.
37. V. F. Sears, *Neutron news*, 1990, **3**, 29-37.
38. B. H. T. a. R. B. V. Dreel, *J. Appl. Cryst.*, 2013, **46**, 554-549.

39. C. Monesi, C. Meneghini, F. Bardelli, M. Benfatto, S. Mobilio, U. Manju and D. D. Sarma, *Nuclear Instruments and Methods in Physics Research Section B: Beam Interactions with Materials and Atoms*, 2006, **246**, 158-164.
40. M. R. Li, D. Walker, M. Retuerto, T. Sarkar, J. Hadermann, P. W. Stephens, M. Croft, A. Ignatov, C. P. Grams, J. Hemberger, I. Nowik, P. S. Halasyamani, T. T. Tran, S. Mukherjee, T. S. Dasgupta and M. Greenblatt, *Angew. Chem. Int. Ed. Engl.*, 2013, **52**, 8406-8410.
41. M. Croft, D. Sills, M. Greenblatt, C. Lee, S. W. Cheong, K. V. Ramanujachary and D. Tran, *Physical Review B*, 1997, **55**, 8726-8732.
42. Y.-H. Huang, G. Liang, M. Croft, M. Lehtimäki, M. Karppinen and J. B. Goodenough, *Chemistry of Materials*, 2009, **21**, 2319-2326.
43. Z. Deng, M. Retuerto, S. Liu, M. Croft, P. W. Stephens, S. Calder, W. Li, B. Chen, C. Jin, Z. Hu, M.-R. Li, H.-J. Lin, T.-S. Chan, C.-T. Chen, S. W. Kim and M. Greenblatt, *Chemistry of Materials*, 2018, **30**, 7047-7054.
44. M.-R. Li, E. E. McCabe, P. W. Stephens, M. Croft, L. Collins, S. V. Kalinin, Z. Deng, M. Retuerto, A. Sen Gupta, H. Padmanabhan, V. Gopalan, C. P. Grams, J. Hemberger, F. Orlandi, P. Manuel, W.-M. Li, C.-Q. Jin, D. Walker and M. Greenblatt, *Nature Communications*, 2017, **8**, 2037.
45. Xiangfan Xu, Lizhen Jiang, Jingqin Shen, Zhangjian Chen and Z. Xu, *Physics Letters A*, 2006, **351**, 431-434.
46. A. Filippetti, and Nicola A. Hill.,, *Physical Review B*, 2002, **65**, 195120.
47. A. W. Sleight and J. F. Weiher, *J. Phys. Chem. Solids.*, 1972, **33**, 679-687.
48. G. Blasse, *Phillips Research Reports*, 1965, **20**, 327-336.
49. A. L. Efros and B. I. Shklovskii, *Journal of Physics C: Solid State Physics*, 1975, **8**, L49.